

Projection-based model-order reduction for unstructured meshes with graph autoencoders

Liam K. Magargal^a, Parisa Khodabakhshi^a, Steven N. Rodriguez^b, Justin W. Jaworski^c, John G. Michopoulos^b

^aDepartment of Mechanical Engineering and Mechanics, Lehigh University, Bethlehem, PA, United States

^bComputational Multiphysics Systems Laboratory, U. S. Naval Research Laboratory, Washington, DC, United States

^cKevin T. Crofton Department of Aerospace and Ocean Engineering, Virginia Tech, Blacksburg, VA, United States

Abstract

This paper presents a graph autoencoder architecture capable of performing projection-based model-order reduction (PMOR) on advection-dominated flows modeled by unstructured meshes. The autoencoder is coupled with the time integration scheme from a traditional deep least-squares Petrov-Galerkin projection and provides the first deployment of a graph autoencoder into a PMOR framework. The presented graph autoencoder is constructed with a two-part process that consists of (1) generating a hierarchy of reduced graphs to emulate the compressive abilities of convolutional neural networks (CNNs) and (2) training a message passing operation at each step in the hierarchy of reduced graphs to emulate the filtering process of a CNN. The resulting framework provides improved flexibility over traditional CNN-based autoencoders because it is extendable to unstructured meshes. To highlight the capabilities of the proposed framework, which is named geometric deep least-squares Petrov-Galerkin (GD-LSPG), we benchmark the method on a one-dimensional Burgers' equation problem with a structured mesh and demonstrate the flexibility of GD-LSPG by deploying it to a two-dimensional Euler equations model that uses an unstructured mesh. The proposed framework provides considerable improvement in accuracy for very low-dimensional latent spaces in comparison with traditional affine projections.

Keywords: Projection-based model-order reduction, Deep LSPG, Geometric deep learning, Graph autoencoders, Unstructured mesh

1. Introduction

Methods in computational mechanics aim to simulate complex physical phenomena via numerical methods. Specifically, approximate solutions are sought by spatially and temporally discretizing the governing model equations of a physical system [1, 2]. In practice, the spatial and temporal resolution must be refined to obtain a sufficiently detailed solution, often resulting in very high-dimensional systems that incur high computational costs. In this context, we define this high-dimensional system as a full-order model (FOM). Projection-based model-order reduction (PMOR) is a class of approximation methods that aims to reduce the computational cost associated with deploying methods in computational mechanics for many-query tasks, such as design optimization, uncertainty quantification, real-time rendering, etc., while preserving sufficient accuracy of the solution [3]. PMOR achieves cost savings by projecting the original high-dimensional computational model (known in this context as the full-order model) onto a precomputed low-dimensional latent space which is computed using data recovered from the FOM in an offline stage. Then, in an online stage, PMOR projects the model equations of the FOM onto a low-dimensional latent space (defined by the dimensionality reduction performed in the offline stage), thereby reducing the operational count complexity of the model and achieving cost savings.

In this study, we are primarily interested in PMOR approaches for methods in computational mechanics that employ unstructured meshes, such as the finite volume method (FVM) and the finite element method. Here, we

Email address: PAK322@lehigh.edu (Parisa Khodabakhshi)

focus on the FVM, but most of our analysis and methods can be applied to the unstructured finite element method as well. The FVM has widespread use in the realms of science and engineering for its ability to conduct high-fidelity simulations of complex physical phenomena [1, 2]. By discretizing the integral forms of governing physical equations, the FVM enables the computation of approximate solutions while preserving conservation laws. Spatial discretization of a domain is typically achieved using one of two main mesh types: structured and unstructured meshes. Structured meshes employ a periodic, grid-like structure to discretize the domain. Conversely, unstructured meshes do not require a grid-like structure and allow mesh components to be arbitrarily ordered [2, 4]. This departure from the grid-like structure grants unstructured meshes a remarkable advantage in representing complex geometries more conveniently, setting them apart from structured meshes. As a result, unstructured meshes are often favored for their ability to handle intricate geometrical configurations with greater ease and accuracy.

Often in engineering applications, obtaining a sufficiently accurate solution via the FVM can incur a computational cost that is prohibitively large. This issue becomes exacerbated in situations where several queries must be made to the FVM simulation. In the many-query settings, PMOR could drastically alleviate the cost of modeling dynamical systems with FVM simulations. Traditionally, PMOR methods rely on projecting the solution onto a low-dimensional latent space via a subspace approximation, such as proper orthogonal decomposition (POD) [5], rational interpolation [6], or balanced truncation [7]. Although affine latent spaces have been leveraged extensively to achieve cost savings for a wide variety of linear and nonlinear models, PMOR procedures employing affine solution manifolds struggle to accurately model advection-dominated flows, which are characterized by sharp gradients and moving shocks and boundaries. Such models exhibit a slowly-decaying Kolmogorov n -width. The Kolmogorov n -width serves as a measure for the error introduced by approximating the solution to a partial differential equation (PDE) with a linear subspace of dimension n [8, 9, 10, 11, 12]. When the decay of the Kolmogorov n -width is slow, the affine latent space used to approximate the solution must be constructed with a high dimension, leading to marginal model reduction. As a result, a great amount of effort has been made to develop reduced-order models (ROMs) for advection-dominated flows, such as adaptive reduced basis schemes [13, 14, 15], segmentation of the domain into multiple reduced-order bases [16], quadratic manifolds [17, 18], and modified POD bases [12, 19].

PMOR has been studied extensively for linear systems [20, 21]. However, for nonlinear dynamical systems, the projection of a system onto a low-dimensional subspace often fails to reduce the computational cost, because through the basic application of projection-based approaches the operational count complexity associated with computing the projection of the nonlinear term scales with the dimension of the original high-dimensional system. As a remedy, some studies employ hyper-reduction methods which introduce an additional layer of approximation to the model, where the nonlinear terms are computed for a selection of sample points and used to update the corresponding low-dimensional states. Such methods include the discrete empirical interpolation method [22, 23, 24], Gauss-Newton with approximated tensors method [25, 26], and energy conserving sampling and weighing method [27]. Alternatively, operator inference aims to bypass the need for introducing an additional layer of approximation via a hyper-reduction scheme by instead learning low-dimensional operators from a regression problem [28, 29, 30]. Furthermore, some methods have coupled the operator inference framework with a lifting transformation suited for nonlinear problems with general nonlinearity by introducing a change of variables to obtain a polynomial form of the model equations [31, 32].

Recently, machine learning has been adopted to overcome the limitations of traditional model reduction when applied to advection-dominated flows with slowly-decaying Kolmogorov n -widths. Historically, autoencoders have been developed to compress and reconstruct input information, such as images [33], but recently autoencoders have been leveraged in engineering applications. Specifically, the model reduction community has used autoencoders to identify a nonlinear mapping between the high-dimensional system and a low-dimensional latent space [34, 35]. Once an autoencoder is trained, the mapping is leveraged to perform online time integration using one of two main classes of approaches. The first class involves training a neural network to approximate the low-dimensional update of the solution at each time step [35, 36, 37, 38, 39] akin to neural ordinary differential equations (ODEs) [40, 41], residual networks [42], and physics-informed neural networks [43]. The second class, and the approach that we adopt in this paper, aims to project the governing equations of the semi-discrete high-dimensional dynamical system onto the low-dimensional latent space using the autoencoder, thereby embedding the physics into the model reduction procedure [44, 45, 46, 47, 48].

A common method used across both classes of machine learning-based ROMs is the convolutional neural network (CNN), which is used to construct low-dimensional solution manifolds [34, 35, 36]. Because CNNs require inputs

to be formulated in a grid structure, the direct application of CNNs to unstructured meshes for the purpose of model reduction is currently untenable. In recent years, graph neural networks (GNNs) have been developed to extract information of interest to the user from sets of unstructured and relational data [49, 50], making them an appropriate method to generate low-dimensional embeddings of models that use unstructured meshes. To date, GNNs have been used to perform dimensional compression with the objective of interpretable latent spaces [51] and used to perform dimensional compression to quickly approximate solutions of parameterized PDEs using a learned operator [52]. The method outlined in this paper, which is named geometric deep least-squares Petrov-Galerkin (GD-LSPG), builds off of the approaches found in [51, 52, 53] to apply graph autoencoders directly into the time integration scheme deployed by the deep least-squares Petrov-Galerkin (dLSPG) framework, a PMOR scheme that leverages CNN-based autoencoders to perform dimensional compression and time integration [46, 47].

The paper is organized in the following manner. Section 2 describes the background and preliminaries of the GD-LSPG framework, which includes the FOM and its corresponding residual minimization scheme, a general formulation of performing nonlinear dimension reduction via autoencoders, and a brief overview of graph theory. Section 3 presents the graph autoencoder deployed in GD-LSPG. Section 4 outlines the time-discrete residual minimizing time integration scheme based on the traditional dLSPG projection. Section 5 presents the results of numerical experiments. Specifically, we apply GD-LSPG to the benchmark one-dimensional (1D) Burgers' equation model using a structured mesh and a two-dimensional (2D) Euler equations model deploying an unstructured mesh. Finally, Section 6 presents conclusions and discusses avenues for future work.

2. Background and Preliminaries

This section presents the background and preliminaries for the GD-LSPG method. Specifically, Section 2.1 introduces the first-order PDE and residual-minimizing time integration scheme on which we develop the GD-LSPG method. Section 2.2 provides a general introduction to performing model reduction and PMOR with an autoencoder, along with some of the current limitations of autoencoders in the literature. Finally, Section 2.3 presents the basics of graph theory to the reader.

2.1. Full-order model

Consider a system of $n_q \in \mathbb{N}$ PDEs where n_q depends on the number of state variables. Using a mesh to spatially discretize the physical domain into $N_c \in \mathbb{N}$ points, the semi-discrete system of the FOM is described by a system of time-continuous ODEs:

$$\frac{d\mathbf{x}}{dt} = \mathbf{f}(\mathbf{x}, t; \boldsymbol{\mu}), \quad \mathbf{x}(0; \boldsymbol{\mu}) = \mathbf{x}^0(\boldsymbol{\mu}), \quad (1)$$

where $\mathbf{x} \in \mathbb{R}^N$ is the semi-discrete state vector, $N = n_q N_c$ denotes the dimension of the FOM, $\boldsymbol{\mu} \in \mathcal{D}$ denotes the parameters, and $\mathbf{f} : \mathbb{R}^N \times (0, T_f] \times \mathcal{D} \rightarrow \mathbb{R}^N$ is the semi-discretized velocity function.

To approximate the time evolution of the state vector, \mathbf{x} , from the system of ODEs, we use the general form in (2),

$$\mathbf{r} : (\boldsymbol{\xi}; \boldsymbol{\mu}) \mapsto \alpha_0 \boldsymbol{\xi} + \sum_{i=1}^{\tau} \alpha_i \mathbf{x}^{n+1-i} + \mathbf{p}(\boldsymbol{\xi}, t; \boldsymbol{\mu}, \Delta t) + \sum_{i=1}^{\tau} \mathbf{q}(\mathbf{x}^{n+1-i}, t; \boldsymbol{\mu}, \Delta t), \quad (2)$$

in which the value of the state vector, \mathbf{x}^{n+1} , at time step $(n+1) \in \mathbb{N}$ is determined by minimizing the time-discrete residual $\mathbf{r} : \mathbb{R}^N \times \mathcal{D} \rightarrow \mathbb{R}^N$ given the state vector at a number of previous time steps, where $\mathbf{p} : \mathbb{R}^N \times (0, T_f] \times \mathcal{D} \times \mathbb{R}_+ \rightarrow \mathbb{R}^N$ and $\mathbf{q} : \mathbb{R}^N \times (0, T_f] \times \mathcal{D} \times \mathbb{R}_+ \rightarrow \mathbb{R}^N$ denote functions defined by the time integration scheme. We note that the time integration scheme is implicit in cases where $\mathbf{p} \neq \mathbf{0}$. In (2), $\alpha_i \in \mathbb{R}$, $i = 0, 1, \dots, \tau$, are constants defined by the time integration scheme, $\boldsymbol{\xi} \in \mathbb{R}^N$ is the sought-after solution of the minimization scheme for the state vector at the $(n+1)$ th time step, the superscript $n+1-i$ denotes the value of the variable at time step $n+1-i \in \mathbb{N}$, $\Delta t \in \mathbb{R}_+$ denotes the time step size, and $\tau \in \mathbb{N}$ is the number of time steps associated with the time integration scheme. The state vector at the $(n+1)$ th time step, \mathbf{x}^{n+1} , is defined as the solution of the minimization problem,

$$\mathbf{x}^{n+1} = \operatorname{argmin}_{\boldsymbol{\xi} \in \mathbb{R}^N} \left\| \mathbf{r}(\boldsymbol{\xi}; \boldsymbol{\mu}) \right\|_2, \quad n = 0, \dots, N_t - 1. \quad (3)$$

where $N_t \in \mathbb{N}$ denotes the final time step, and the time step is chosen to be fixed, i.e., $\Delta t_n = \Delta t$, and $t_n = n\Delta t$. With an appropriate selection of coefficients α_i and functions \mathbf{p} and \mathbf{q} , the general formulation of (2) will cover forward and backward Euler schemes, as well as Runge-Kutta schemes.

2.2. Nonlinear dimension reduction via autoencoders

A wide variety of nonlinear mappings have been adopted in the literature in recent years to obtain a low-dimensional latent space for PMOR on nonlinear problems. A common approach is to leverage autoencoders to approximate a mapping between the high-dimensional system and the low-dimensional latent space [18, 46, 47, 54, 55, 56]. Autoencoders are a type of deep learning architecture in which the basic idea is to perform dimensional compression on a data set, in our case a FVM state vector, down to a latent space with an encoder, $\mathbf{Enc} : \mathbf{x} \mapsto \hat{\mathbf{x}}$ with $\mathbf{Enc} : \mathbb{R}^N \rightarrow \mathbb{R}^M$, and to reconstruct the data set by decoding the latent space with a decoder, $\mathbf{Dec} : \hat{\mathbf{x}} \mapsto \mathbf{x}$ with $\mathbf{Dec} : \mathbb{R}^M \rightarrow \mathbb{R}^N$, where $M \ll N$. The former is a nonlinear mapping from the high-dimensional state vector, \mathbf{x} , to the low-dimensional latent representation, $\hat{\mathbf{x}}$, and the latter is a nonlinear mapping from the low-dimensional embedding to the high-dimensional state vector.

The encoder and decoder are constructed by a series of layers in which each layer applies a set of predefined functions to the output of the previous layer. The nonlinearity associated with the mapping is introduced through an appropriate selection of functions. General forms of the encoder and decoder, consisting of $n_h \in \mathbb{N}$ and $n_g \in \mathbb{N}$ layers, respectively, are,

$$\mathbf{Enc} : (\mathbf{x}; \theta) \mapsto \mathbf{h}_{n_h}(\cdot; \Theta_{n_h}) \circ \mathbf{h}_{n_h-1}(\cdot; \Theta_{n_h-1}) \circ \dots \circ \mathbf{h}_2(\cdot; \Theta_2) \circ \mathbf{h}_1(\mathbf{x}; \Theta_1), \quad (4)$$

$$\mathbf{Dec} : (\hat{\mathbf{x}}; \omega) \mapsto \mathbf{g}_{n_g}(\cdot; \Omega_{n_g}) \circ \mathbf{g}_{n_g-1}(\cdot; \Omega_{n_g-1}) \circ \dots \circ \mathbf{g}_2(\cdot; \Omega_2) \circ \mathbf{g}_1(\hat{\mathbf{x}}; \Omega_1), \quad (5)$$

where $\mathbf{h}_i(\cdot; \Theta_i)$, $i = 1, \dots, n_h$ and $\mathbf{g}_i(\cdot; \Omega_i)$, $i = 1, \dots, n_g$ denote the function(s) acting on the input of the i^{th} layer of the encoder and decoder networks, respectively, (or equivalently the output of the corresponding $(i - 1)^{\text{th}}$ layer). As will be explained later in Sections 3.2 and 3.3, some layers encompass a number of functions, depending on their objective, which will collectively form $\mathbf{h}_i(\cdot; \Theta_i)$ or $\mathbf{g}_i(\cdot; \Omega_i)$. In (4) and (5), Θ_i , $i = 1, \dots, n_h$ and Ω_i , $i = 1, \dots, n_g$, denote the weights and biases of the i^{th} layer of the encoder and decoder networks, respectively. The set of all the weights and biases of the autoencoder, i.e., $\theta := \{\Theta_1, \dots, \Theta_{n_h}\}$ and $\omega := \{\Omega_1, \dots, \Omega_{n_g}\}$, are trained to minimize an appropriately defined error norm between the input to the encoder and the output of the decoder. In this manuscript, we use an equal number of layers for the encoder and decoder, i.e., $n_h = n_g = n_\ell$.

Due to their remarkable ability to filter grid-based information, across extensive amounts of literature in PMOR [34, 35, 36, 46, 47, 57], CNNs have been heavily relied upon as the backbone for developing autoencoder architectures. However, CNNs are inherently dependent upon the domain inputs being formulated as a structured grid, meaning that PMOR methods leveraging CNNs are not readily applicable to unstructured meshes (see Figure 1).

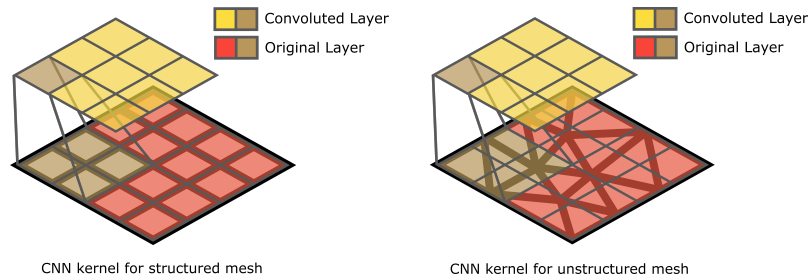


Figure 1: Visualization of CNN kernel attempting to perform dimensional compression upon a structured mesh (left) and an unstructured mesh (right). Note that the structured nature of the CNN kernel enables direct dimensional compression upon a structured mesh, but renders it not readily applicable to unstructured meshes.

Our proposed method overcomes the need for structured meshes to perform PMOR with a nonlinear projection using autoencoders. Our goal is to generalize autoencoder-based PMOR methods such that both structured and unstructured meshes can be inputs to the autoencoder (see Figure 2). Given that unstructured meshes are commonly used in engineering applications to represent complex geometry, our approach can be widely extended to applications

with arbitrary topology. Our proposed architecture follows an outline that is similar to graph U-nets [53], multiscale graph autoencoders [51], and graph convolutional autoencoders for parameterized PDEs [52], wherein a hierarchy of graphs is generated, each with fewer nodes than the previous level.

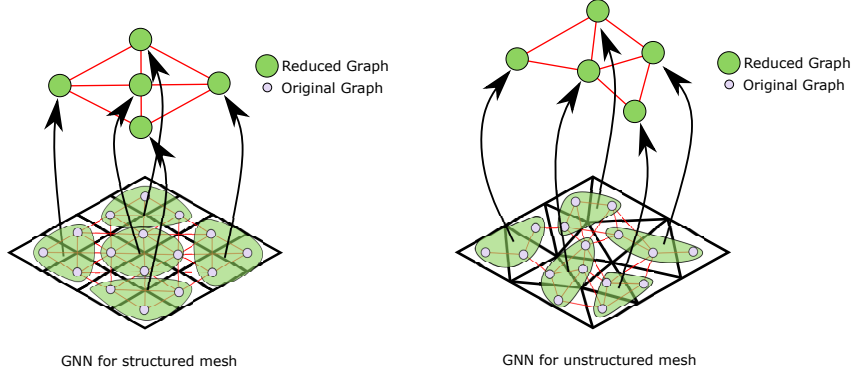


Figure 2: Visualization of graph autoencoder performing dimensional compression upon a structured mesh (left) and an unstructured mesh (right). Note that the graph autoencoder framework for dimensional compression is flexible and generalizable to both cases, unlike CNNs.

2.3. Graph theory

Extensive reading on graph theory can be found in the works of Hamilton [58] and Battaglia et al. [49], but a brief overview is provided in this section to provide sufficient background for our graph autoencoder architecture. A graph is a tuple $\mathcal{G} = \{\mathcal{V}, \mathcal{E}\}$, where \mathcal{V} denotes the node set, $|\mathcal{V}|$ denotes the number of nodes in the graph, and \mathcal{E} denotes the edge set, which is chosen to represent user-prescribed relationships between the nodes in the node set. Depending on the application, the graph (and the associated node set and edge set) can be used to represent a wide variety of concepts. For example, molecules can be modeled as a graph by representing atoms as nodes and bonds as edges [59], while social networks can be modeled as a graph by representing people as nodes and friendships as edges [60].

The adjacency matrix, $\mathbf{A} = [a_{ij}] \in \mathbb{R}^{|\mathcal{V}| \times |\mathcal{V}|}$, is another way to represent the edge set of a graph. Consider the case where the nodes are indexed by a number, $i = 1, \dots, |\mathcal{V}|$. If nodes i and j in the graph are connected via an edge, i.e., for $i, j \in \mathcal{V}$, we have $(i, j) \in \mathcal{E}$, the corresponding entry in the adjacency matrix is $a_{ij} = 1$. Otherwise, we have $a_{ij} = 0$. In this manuscript, we consider exclusively undirected graphs, meaning for any edge in the graph, $(i, j) \in \mathcal{E}$, we also have $(j, i) \in \mathcal{E}$. With this formulation, our adjacency matrix will be symmetric. A visualization of the construction of the adjacency matrix for a given graph is found in Figure 3.

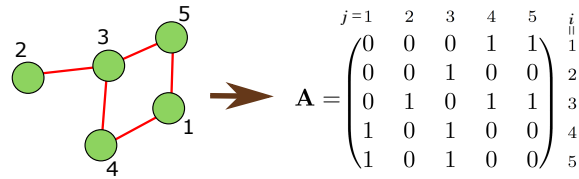


Figure 3: Formation of the adjacency matrix from a given graph.

A node feature matrix, $\mathbf{X} \in \mathbb{R}^{|\mathcal{V}| \times N_F}$, can be utilized to prescribe feature information to the node set of the graph, where the i^{th} row of \mathbf{X} denotes the node feature vector of the i^{th} node in the graph, and $N_F \in \mathbb{N}$ denotes the number of features prescribed to each node.

3. Dimension reduction via graph autoencoders

In this section, we develop the specifics of the graph autoencoder used in GD-LSPG. Again, we emphasize that although we study GD-LSPG in the context of the FVM, it remains applicable to a variety of numerical methods in computational mechanics, such as the finite element method.

Upon spatial discretization of the physical domain, each finite volume cell is represented by a node (which is different from the vertices of the cell). We take the node set \mathcal{V} to represent the cells in the discretized domain, i.e., $|\mathcal{V}| = N_c$. To emulate the manner in which CNNs filter information from neighboring grid points in the spatial discretization, we take the edge set, \mathcal{E} , to connect the node representation of cells within a user-defined radius of each other, i.e.,

$$\mathcal{E} = \mathbf{Radius_Graph}(\mathbf{Pos}, r) = \{ \forall (j, k) : j, k \in \mathcal{V}, \|\mathbf{Pos}_j - \mathbf{Pos}_k\| \leq r \}, \quad (6)$$

where $\mathbf{Pos} \in \mathbb{R}^{N_c \times n_d}$ is the matrix denoting the spatial positions of the node-representation of the cells in the FVM discretization, taken as the cell-centroids (i.e., for triangular mesh elements, the average position of the vertices) of the finite volume cells. Row j of the matrix (i.e., \mathbf{Pos}_j) denotes the position of node $j \in \mathcal{V}$, $n_d \in \mathbb{N}$ denotes the spatial dimensionality of the modeled problem, j and k denote the indices of the corresponding nodes in the node set, $r \in \mathbb{R}$ denotes the user-defined radius, and $\|\cdot\| : \mathbb{R}^{n_d} \rightarrow \mathbb{R}_+$ denotes the Euclidean norm. The adjacency matrix is used to represent the edge set in a matrix format.

The feature matrix, $\mathbf{X} \in \mathbb{R}^{N_c \times n_q}$ is a matrix with the number of rows equal to the number of cells in the FVM discretization, i.e., N_c , and the number of columns equal to the number of state variables in the governing PDE, n_q . In other words, the feature matrix \mathbf{X} is the matrix version of the state vector $\mathbf{x} \in \mathbb{R}^N$ (with $N = n_q N_c$) introduced in Section 2. As a result, the formulation has a direct mapping between the state vector \mathbf{x} and the node feature matrix \mathbf{X} (**Matricize** : $\mathbf{x} \mapsto \mathbf{X}$, with **Matricize** : $\mathbb{R}^{N_c \cdot n_q} \rightarrow \mathbb{R}^{N_c \times n_q}$) and a direct mapping between the node feature matrix \mathbf{X} and the state vector \mathbf{x} (**Vectorize** : $\mathbf{X} \mapsto \mathbf{x}$, with **Vectorize** : $\mathbb{R}^{N_c \times n_q} \rightarrow \mathbb{R}^{N_c \cdot n_q}$).

Once a graph representation of a solution state is formulated, it can be encoded to a latent representation with a graph autoencoder following the general form of (4)-(5). In the subsequent sections, we present the graph autoencoder used in the GD-LSPG framework and the specifics of the architecture of the encoder and the decoder. First, Section 3.1 presents a hierarchical spectral clustering algorithm used by the autoencoder to generate a hierarchy of reduced graphs to emulate the compressive abilities of CNNs. Next, Section 3.2 details the encoder architecture and its deployment of the hierarchy of reduced graphs to create a low-dimensional embedding of the input graph. Then, Section 3.3 details the decoder architecture and its deployment of the hierarchy of reduced graphs in reverse order to reconstruct the original input graph from its latent representation. In our graph autoencoder, we include an additional layer with no trainable parameters for preprocessing and postprocessing in the encoder (Section 3.2.1) and the decoder (Section 3.3.3), respectively. Finally, Section 3.4 presents the training strategy deployed to optimize the training parameters of the encoder and decoder. Figure 4 provides a visual representation of the graph autoencoder deployed in GD-LSPG, with $n_\ell = 3$ for demonstration purposes.

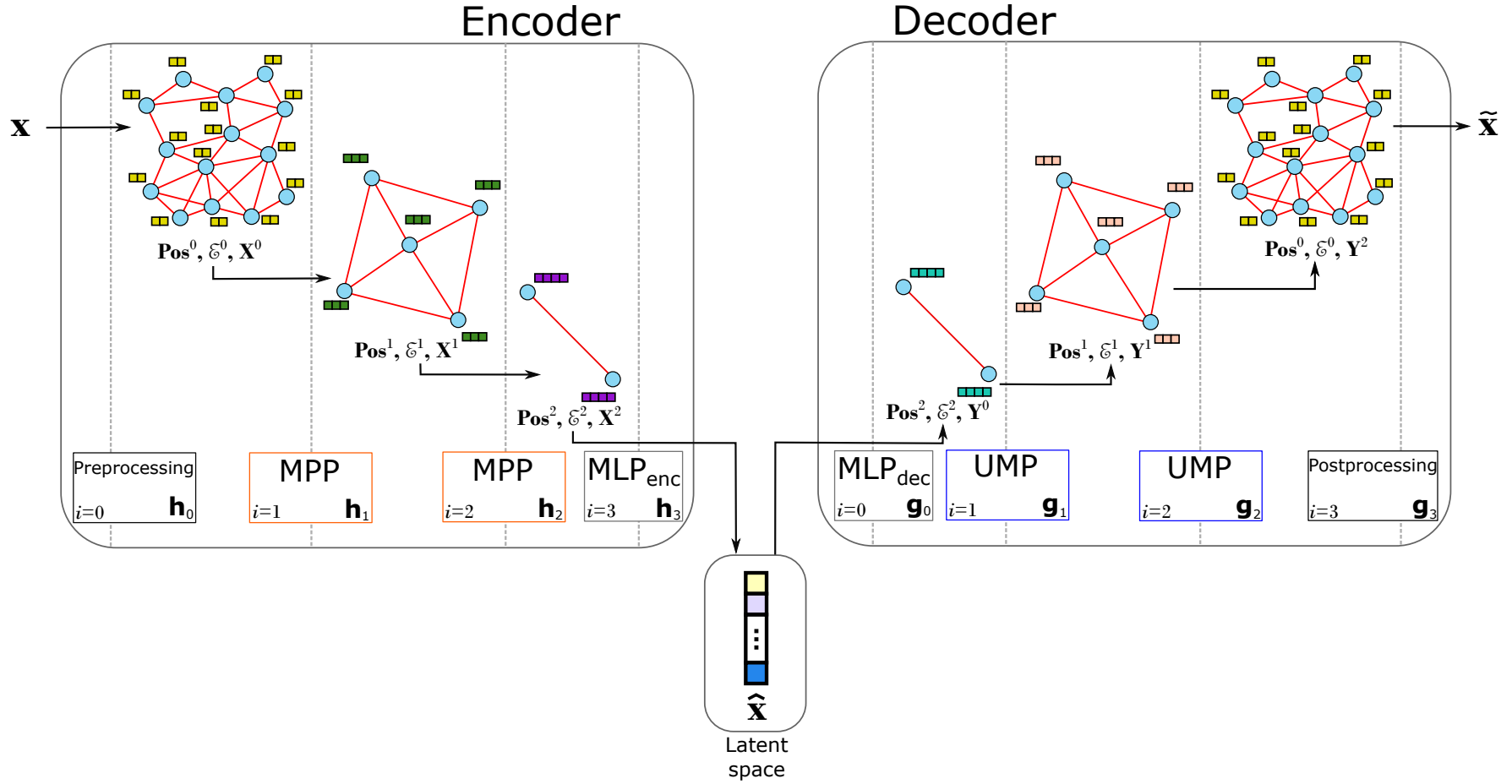


Figure 4: Graph autoencoder architecture deployed in GD-LSPG. Vertical dotted lines represent the separation between layers in the hierarchy of reduced graphs. Boxes over the vertical dotted lines at the bottom of the figure represent specific layers of the autoencoder described in this section. The encoder is the trained mapping between the high-dimensional state and the low-dimensional latent space. The encoder is comprised of a preprocessing layer to model the input state vector as a graph, followed by a series of trained message passing and pooling (MPP) layers to reduce the number of nodes in the graph, then a flattening and fully-connected/multilayer perceptron (MLP) layer. The resulting low-dimensional state vector is sent to the decoder, which is the trained mapping between the low-dimensional latent space and the reconstructed high-dimensional state. The decoder is comprised of a fully-connected/MLP layer, followed by a series of UMP layers to increase the number of nodes in the graph, and then a postprocessing layer to prepare the output for deployment in the time integration scheme. Note that the superscript i in \mathbf{Pos}^i and \mathcal{E}^i represents the graph number in the hierarchy of graphs with $i = 0$ denoting the original graph representing the discretized mesh.

3.1. Generating a hierarchy of reduced graphs with spectral clustering

To compute a hierarchy of reduced graphs for the autoencoder used in GD-LSPG, at each level in the hierarchy, we aim to partition the graph into a pre-defined number of non-overlapping sets of strongly connected nodes. We then use the partitions to aggregate each cluster of nodes together into a single node at the next layer of the hierarchy, thereby reducing the number of nodes in the graph and the total dimension of the graph.

We consider the case where the encoder and the decoder each have $n_\ell \in \mathbb{N}$ layers. As will be presented in the subsequent sections, the encoder and decoder both have a fully-connected/MLP layer along with $n_\ell - 1$ layers with compressed graphs. Therefore, in this section, we aim to produce a hierarchy of reduced graphs composed of $n_\ell - 1$ reduced graphs that result in a hierarchy of n_ℓ graphs, including the input graph of the discretized FOM (i.e., graph 0). The graphs in the encoder and the decoder will have the same topology but with reverse ordering. This means that the i^{th} graph in the hierarchy of the graphs of the encoder, $i = 0, \dots, n_\ell - 1$, will be equivalent to the $(n_\ell - i - 1)^{\text{th}}$ graph of the decoder (refer to Figure 4). In other words, the first graph of the decoder is the $(n_\ell - 1)^{\text{th}}$ (final) graph of the encoder, and the final graph of the decoder is the zeroth (original) graph of the encoder. Hence, we focus on building the hierarchy of the graphs for the encoder. This task can be achieved by minimizing the number of ‘broken’ edges in the graph topology of the $(i - 1)^{\text{th}}$ layer to form the clusters for the i^{th} layer’s graph. The graph representation of the FOM, $\mathcal{G}^0 = (\mathcal{V}^0, \mathcal{E}^0)$ are given from (6) using the discretized mesh of the FOM. In addition, the number of nodes in the layers $i = 1, \dots, n_\ell - 1$, i.e., $\{|\mathcal{V}^1|, |\mathcal{V}^2|, \dots, |\mathcal{V}^{n_\ell-1}|\}$, along with the radius used in (6), i.e., $\{r^0, r^1, \dots, r^{n_\ell-1}\}$, are prescribed *a priori*, dictating the amount of reduction performed and the number of edges at each layer in the hierarchy.

At layer $i \in \{1, \dots, n_\ell - 1\}$ of the encoder, we aim to reduce the number of nodes from $|\mathcal{V}^{i-1}|$ in layer $i - 1$ to $|\mathcal{V}^i|$ in layer i with $|\mathcal{V}^i| < |\mathcal{V}^{i-1}|$. This action is first carried out by forming $|\mathcal{V}^i|$ clusters, i.e., $\mathcal{A}_1^{i-1}, \mathcal{A}_2^{i-1}, \dots, \mathcal{A}_{|\mathcal{V}^i|}^{i-1}$ with the following conditions,

$$\begin{cases} |\mathcal{A}_j^{i-1}| \geq 1, & j = 1, \dots, |\mathcal{V}^i| \\ \mathcal{A}_j^{i-1} \subset \mathcal{V}^{i-1}, & j = 1, \dots, |\mathcal{V}^i| \\ \mathcal{A}_j^{i-1} \cap \mathcal{A}_k^{i-1} = \emptyset, & j \neq k, j, k = 1, \dots, |\mathcal{V}^i| \\ \mathcal{A}_1^{i-1} \cup \mathcal{A}_2^{i-1} \cup \dots \cup \mathcal{A}_{|\mathcal{V}^i|}^{i-1} = \mathcal{V}^{i-1}, \end{cases} \quad (7)$$

which ensures that all clusters are a non-empty subset of the node set of layer $i - 1$, the intersection of any two distinct clusters is the empty set, and the union of all clusters is equal to the node set of layer $i - 1$. In (7), $|\cdot|$ denotes the cardinality of the set. For given clusters $\mathcal{A}_1^{i-1}, \mathcal{A}_2^{i-1}, \dots, \mathcal{A}_{|\mathcal{V}^i|}^{i-1}$, we evaluate the function,

$$\mathbf{RatioCut} : (\mathcal{V}^{i-1}, \mathcal{E}^{i-1}) \mapsto \frac{1}{2} \sum_{k=1}^{|\mathcal{V}^i|} \frac{|\mathcal{V}(u, v) \in \mathcal{E}^{i-1} : u \in \mathcal{A}_k^{i-1}, v \in \bar{\mathcal{A}}_k^{i-1}|}{|\mathcal{A}_k^{i-1}|}, \quad (8)$$

that tends to measure the number of broken edges for the given cluster choice, where \mathcal{E}^{i-1} denotes the edge set of the graph at the $(i - 1)^{\text{th}}$ level in the hierarchy, (u, v) represents any existing edge in \mathcal{E}^{i-1} connecting nodes u and v , $\mathcal{A}_k^{i-1} \subset \mathcal{V}^{i-1}$ denotes a subset of nodes in the graph at the $(i - 1)^{\text{th}}$ level in the hierarchy and $\bar{\mathcal{A}}_k^{i-1} = \mathcal{V}^{i-1} \setminus \mathcal{A}_k^{i-1}$ denotes the complement of the set \mathcal{A}_k^{i-1} at the same level.

The number of distinct ways we can choose $|\mathcal{V}^i|$ clusters from $|\mathcal{V}^{i-1}|$ nodes while satisfying conditions of (7) is determined from the Stirling number of the second kind [61], $S(n, k) = \frac{1}{k!} \sum_{j=0}^k (-1)^j \binom{k}{j} (k - j)^n$ with $n = |\mathcal{V}^{i-1}|$ and $k = |\mathcal{V}^i|$. The optimal cluster is the one with the minimum value for the function **RatioCut** from (8). However, this minimization problem is NP-hard [58, 62]. As discussed in Von Luxburg [62], spectral clustering introduces a relaxation on the minimization problem to eliminate its discrete nature. The departure from a discrete set allows the user to perform an eigenvalue analysis on the graph to generate the clusters appropriately.

The spectral clustering algorithm from Hamilton [58] is leveraged in this study and can be found in Algorithm 1, where $\mathbf{Pos}^i \in \mathbb{R}^{|\mathcal{V}^i| \times n_u}$ denotes the matrix of spatial coordinates for the graph at the i^{th} level in the hierarchy, \mathbf{A}^i is the adjacency matrix of the i^{th} layer in the hierarchy generated by the edge index, \mathcal{E}^i , of layer i , previously defined in (6), $r^i \in \mathbb{R}_+$ denotes a user-prescribed radius to be used in (6), $\mathbf{S}^i \in \mathbb{R}^{|\mathcal{V}^i| \times |\mathcal{V}^{i+1}|}$ denotes the assignment matrix of the i^{th} layer of the hierarchy which is used to assign each node in layer i to a cluster in layer $i + 1$, and thus a portion of a single node at the layer $i + 1$ in the hierarchy. The assignment matrix is used to cluster and decrease the number of nodes in

the graph at each step in the hierarchy of reduced graphs. In the algorithm, $\mathbf{D}^i \in \mathbb{R}^{|\mathcal{V}^i| \times |\mathcal{V}^i|}$ is the diagonal degree matrix representing the number of edges connected to each node in the i^{th} layer of the hierarchy, $\mathbf{L}^i = \mathbf{D}^i - \mathbf{A}^i$ is the Laplacian of the graph associated with the i^{th} layer in the hierarchy, $\mathbf{B}^i \in \mathbb{R}^{|\mathcal{V}^i| \times |\mathcal{V}^{i+1}|}$ denotes the spectral node feature matrix formed by the $|\mathcal{V}^{i+1}|$ smallest eigenvectors of \mathbf{L}^i , excluding the smallest. According to [62], the smallest eigenvalue of the unnormalized Laplacian is simply zero and can therefore be neglected. As dimensional compression is performed in the hierarchy of reduced graphs, the nodes of the graphs deeper in the hierarchy tend to become closer together due to the nature of the positions of each node being computed based on the arithmetic mean of their corresponding cluster in the previous layer. To avoid the natural accumulation of the nodes to a smaller spatial domain, a rescaling operator, i.e., **Rescale** : $\mathbb{R}^{|\mathcal{V}^{i+1}| \times n_d} \rightarrow \mathbb{R}^{|\mathcal{V}^{i+1}| \times n_d}$ is used at each layer to rescale \mathbf{Pos}^{i+1} such that the maximum and minimum values of the coordinates match that of the previous layer in the hierarchy. This algorithm is visually represented in Figure 5.

The construction of the hierarchy of reduced graphs is performed in the offline stage given the original mesh, number of layers, the user-prescribed values for the number of nodes in the graphs of each layer, i.e., $|\mathcal{V}^i|$ for $i = 1, \dots, n_\ell - 1$, and the user-prescribed values for radii used in (6), i.e., $r^0, r^1, \dots, r^{n_\ell-1}$. While the hierarchy of graphs will be utilized in the encoder and decoder, the architecture of the encoder and decoder does not influence the spectral clustering step.

Algorithm 1: Hierarchical spectral clustering for graph reduction

Inputs: $\mathbf{Pos}^0, n_\ell, |\mathcal{V}^1|, \dots, |\mathcal{V}^{n_\ell-1}|, r^0, \dots, r^{n_\ell-1}$

Outputs: $\mathcal{E}^0, \dots, \mathcal{E}^{n_\ell-1}, \mathbf{S}^0, \dots, \mathbf{S}^{n_\ell-2}, \mathbf{Pos}^1, \dots, \mathbf{Pos}^{n_\ell-1}$

Initialize $i \leftarrow 0$;

Initialize $\mathcal{E}^0 \leftarrow \mathbf{Radius_Graph}(\mathbf{Pos}^0, r^0)$;

while $i < n_\ell - 1$ **do**

1. Compute the adjacency matrix, \mathbf{A}^i , from \mathcal{E}^i ;
2. Compute the graph Laplacian, $\mathbf{L}^i \leftarrow \mathbf{D}^i - \mathbf{A}^i$;
3. Form the spectral node feature matrix, $\mathbf{B}^i \in \mathbb{R}^{|\mathcal{V}^i| \times |\mathcal{V}^{i+1}|}$, with the $|\mathcal{V}^{i+1}|$ smallest eigenvectors of \mathbf{L}^i (excluding the smallest) as its columns;
4. Perform K-means clustering (See [63] for further details) on the spectral node features (i.e., the rows of \mathbf{B}^i);
5. Using the clusters computed by the K-means clustering, generate the assignment matrix, $\mathbf{S}^i \in \mathbb{R}^{|\mathcal{V}^i| \times |\mathcal{V}^{i+1}|}$, such that each node in the $(i + 1)^{\text{th}}$ layer is equivalent to the arithmetic mean of its corresponding cluster's positions in the i^{th} layer;
6. $\mathbf{Pos}^{i+1} \leftarrow \mathbf{Rescale}(\mathbf{S}^i \mathbf{Pos}^i)$;
7. Compute the edge set for layer $i + 1$ based on nearest neighbors within the radius r^{i+1} ,
 $\mathcal{E}^{i+1} \leftarrow \mathbf{Radius_Graph}(\mathbf{Pos}^{i+1}, r^{i+1})$;
8. $i \leftarrow i + 1$;

end

3.2. Encoder architecture

The encoder architecture deploys the hierarchy of reduced graphs computed via the procedure from Section 3.1. The encoder consists of layers $i = 0, \dots, n_\ell$. The zeroth layer ($i = 0$), outlined in Section 3.2.1, is a preprocessing layer that tailors the input data \mathbf{x} to the form suited for the graph autoencoder. Layers $i = 1, \dots, n_\ell - 1$, outlined in Section 3.2.2, leverage the hierarchy of reduced graphs from Section 3.1 to perform message passing and pooling (MPP) operations that reduce the dimension of the system. The final layer of the encoder ($i = n_\ell$), as outlined in Section 3.2.3, utilizes an MLP to arrive at the low-dimensional embedding $\hat{\mathbf{x}}$.

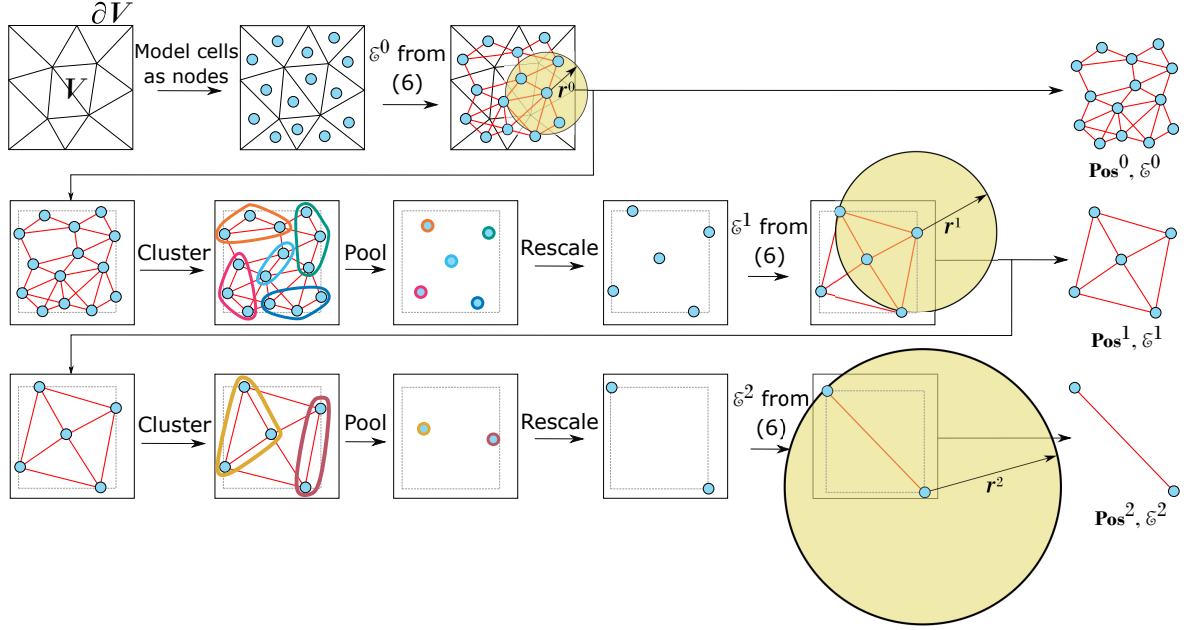


Figure 5: A visual representation of Algorithm 1 for generating a hierarchy of reduced meshes. The input mesh (top left, generated for a domain V and its boundary ∂V represented by the solid black box) is modeled as the layer “0” graph in which the cell centroids of the discretized domain form the node set \mathcal{V}^0 , and the edge set \mathcal{E}^0 (and subsequently the associated adjacency matrix \mathbf{A}^0) are determined from (6) by determining the nodes that fall within r^0 distance of each other. At layer i ($i = 1, \dots, n_\ell - 1$), nodes are partitioned into clusters using a spectral clustering algorithm to achieve a dimensionally-reduced graph from that of layer $i - 1$. The nodal positions of the graph of layer i , obtained from the arithmetic mean position of node clusters from layer $i - 1$, are rescaled to ensure that the maximum and minimum coordinates of the nodes in graph layer i are equal to those of layer $i - 1$, where the maximum and minimum values of the x and y coordinates are represented by the grey dotted box. Finally, the edge set of the reduced graph of layer i , i.e., \mathcal{E}^i , is determined from (6).

3.2.1. Preprocessing – Layer 0

The preprocessing layer of the encoder ($i = 0$) encompasses two operators, **Matricize** and **Scale**, acting on the input vector \mathbf{x} . For a FOM with n_q state variables, the **Matricize** operator is used to convert $\mathbf{x} \in \mathbb{R}^{n_q N_c}$ to the node feature matrix $\mathbf{X} \in \mathbb{R}^{N_c \times n_q}$ in which each column of the matrix represents the nodal values of one state variable. If the FOM consists of only one state variable (i.e., $n_q = 1$), $\mathbf{X} = \mathbf{x}$, and the **Matricize** operator will be the identity operator. As defined in (9), the **Scale** operator acts on the resulting node feature matrix to improve the numerical stability of training, as is commonly performed in the literature [46, 47],

$$\mathbf{Scale} : \mathbf{X}_{ij}^0 \mapsto \frac{\mathbf{X}_{ij}^0 - \mathcal{X}_j^{\min}}{\mathcal{X}_j^{\max} - \mathcal{X}_j^{\min}}, \quad i = 1, \dots, N_c, \quad j = 1, \dots, n_q \quad (9)$$

where **Scale** : $\mathbb{R} \rightarrow [0, 1]$ is an element-wise scaling operator acting on the elements of \mathbf{X} , and $\mathcal{X}_j^{\max}, \mathcal{X}_j^{\min} \in \mathbb{R}$ denote the maximum and minimum values, respectively, of the j^{th} feature (i.e., j^{th} column of matrix \mathbf{X}) in the solution states used to train the autoencoder, which are determined and stored before training begins. The resulting form of the preprocessing layer is

$$\mathbf{h}_0 : (\mathbf{x}; \Theta_0) \mapsto \mathbf{Scale}(\cdot) \circ \mathbf{Matricize}(\mathbf{x}), \quad (10)$$

where $\mathbf{h}_0 : \mathbb{R}^{N_c n_q} \rightarrow \mathbb{R}^{N_c \times n_q}$, and $\Theta_0 = \emptyset$ is the empty set, as the preprocessing layer does not have trainable weights and biases.

3.2.2. Message passing and pooling (MPP) – Layers 1, . . . , n_ℓ – 1

The MPP layer consists of two processes, where each relies upon the hierarchy of reduced graphs computed in Section 3.1. The first operation is a message passing operation, wherein nodes connected by an edge exchange information with each other to obtain information about nearby nodes. The optimal information exchange is obtained from training the autoencoder. In the encoder, the message passing operation in layer i increases the number of features associated with each node from $N_F^{i-1} \in \mathbb{N}$ to $N_F^i \in \mathbb{N}$. We take our message passing operation to be a mean aggregation SAGEConv from Hamilton et al. [64], which applies updates to each node based on the arithmetic mean of its neighbors’ features, i.e.,

$$\mathbf{MP}_{\text{enc}}^i : (\mathbf{X}^{i-1}; \Theta_i) \mapsto \sigma \left(\mathbf{X}_j^{i-1} \mathbf{W}_1^i + \left(\text{mean}_{n \in \mathcal{K}^{i-1}(j)} \mathbf{X}_n^{i-1} \right) \mathbf{W}_2^i \right), \quad j = 1, \dots, |\mathcal{V}^{i-1}|, \quad (11)$$

with $\mathbf{MP}_{\text{enc}}^i : \mathbb{R}^{|\mathcal{V}^{i-1}| \times N_F^{i-1}} \times \mathbb{R}^{N_F^{i-1} \times N_F^i} \times \mathbb{R}^{N_F^{i-1} \times N_F^i} \rightarrow \mathbb{R}^{|\mathcal{V}^{i-1}| \times N_F^i}$, where $\mathbf{X}^{i-1} \in \mathbb{R}^{|\mathcal{V}^{i-1}| \times N_F^{i-1}}$ denotes the input node feature matrix to the i^{th} layer, the subscripts j and n denote the j^{th} and n^{th} rows of \mathbf{X}^{i-1} , $\mathbf{W}_1^i, \mathbf{W}_2^i \in \mathbb{R}^{N_F^{i-1} \times N_F^i}$ denote the weights with $\Theta_i = \{\mathbf{W}_1^i, \mathbf{W}_2^i\}$ denoting the set of weights for the i^{th} MPP layer, $\mathcal{K}^{i-1}(j)$ denotes the set of nodes connected to node j based on the adjacency matrix \mathbf{A}^{i-1} , where $j \in \mathbb{N}$ denotes the j^{th} node in the graph at layer $i - 1$, and $\sigma : \mathbb{R} \rightarrow \mathbb{R}$ denotes the element-wise activation function, chosen here to be the exponential linear unit (ELU) due to its continuously differentiable property [65]. The SAGEConv function described in (11), includes a loop over all nodes $j \in \mathcal{V}^{i-1}$, where for each node, the j^{th} row of the output $\bar{\mathbf{X}}^{i-1}$ of the message passing operation is calculated. The output of (11) has the same number of rows as its input, \mathbf{X}^{i-1} , but can have a different number of features (i.e., N_F^i not necessarily equal to N_F^{i-1}).

The next step of the MPP layer is a pooling operation. In the pooling operation, the assignment matrices from Section 3.1 are used to reduce the number of nodes in a graph. By construction, the assignment matrices are equivalent to an arithmetic mean operation. As a result, we use them to compute the arithmetic mean feature vector of each cluster to get \mathbf{X}^i , i.e.,

$$\mathbf{Pool}^i : (\bar{\mathbf{X}}^{i-1}) \mapsto (\mathbf{S}^{i-1})^T \bar{\mathbf{X}}^{i-1}, \quad (12)$$

with $\mathbf{Pool}^i : \mathbb{R}^{|\mathcal{V}^{i-1}| \times N_F^i} \rightarrow \mathbb{R}^{|\mathcal{V}^i| \times N_F^i}$, where $\bar{\mathbf{X}}^{i-1} \in \mathbb{R}^{|\mathcal{V}^{i-1}| \times N_F^i}$ denotes the output of the message passing operation, $\mathbf{MP}_{\text{enc}}^i$, and $\mathbf{S}^{i-1} \in \mathbb{R}^{|\mathcal{V}^{i-1}| \times |\mathcal{V}^i|}$ is the assignment matrix precomputed by the spectral clustering algorithm in Section 3.1. The full MPP layer takes the form,

$$\mathbf{h}_i : (\mathbf{X}^{i-1}; \Theta_i) \mapsto \mathbf{Pool}^i(\cdot) \circ \mathbf{MP}_{\text{enc}}^i(\mathbf{X}^{i-1}; \Theta_i), \quad (13)$$

with $\mathbf{h}_i : \mathbb{R}^{|\mathcal{V}^{i-1}| \times N_F^{i-1}} \times \mathbb{R}^{N_F^{i-1} \times N_F^i} \times \mathbb{R}^{N_F^{i-1} \times N_F^i} \rightarrow \mathbb{R}^{|\mathcal{V}^i| \times N_F^i}$. Hence, the MPP layer, as visually represented in Figure 6, decreases the number of nodes in a given graph and increases the number of features associated with each node.

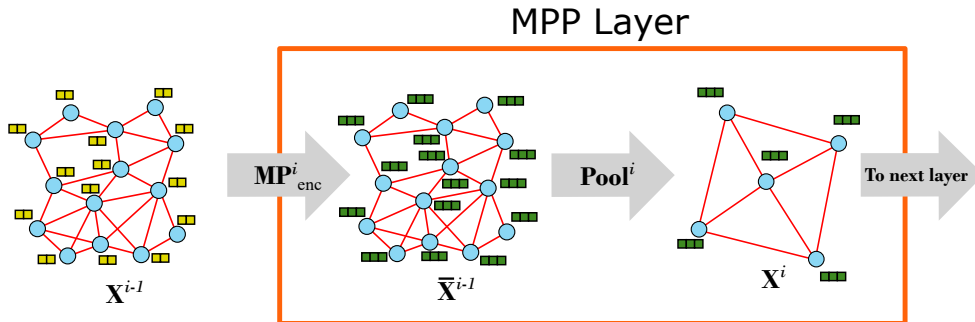


Figure 6: MPP layer used in the encoder of our graph autoencoder. The layer accepts a graph as input and performs message passing to exchange information between locally connected nodes. Next, the graph nodes are pooled together based on their clusters from the hierarchical spectral clustering algorithm. This pooling operation reduces the number of nodes in the graph to perform dimensional compression.

3.2.3. Fully-connected layer: compression – Layer n_ℓ

In the final layer of the encoder ($i = n_\ell$), we first flatten the input matrix $\mathbf{X}^{n_\ell-1} \in \mathbb{R}^{|\mathcal{V}^{n_\ell-1}| \times N_F^{n_\ell-1}}$ to a vector-representation, i.e., **Flatten** : $\mathbf{X}^{n_\ell-1} \mapsto \bar{\mathbf{x}}^{n_\ell-1}$, where $\bar{\mathbf{x}}^{n_\ell-1} \in \mathbb{R}^{|\mathcal{V}^{n_\ell-1}| N_F^{n_\ell-1}}$. Here, we note that the **Flatten** operator is similar to the **Vectorize** operator, but with dimensions different than the node feature matrix of the full-order solution. Next, a fully-connected/MLP layer is applied to the flattened state to compress it to a low-dimensional vector representation, i.e.,

$$\mathbf{MLP}_{\text{enc}} : (\bar{\mathbf{x}}^{n_\ell-1}; \Theta_{n_\ell}) \mapsto \mathbf{W}^{n_\ell} \bar{\mathbf{x}}^{n_\ell-1} + \mathbf{b}^{n_\ell}, \quad (14)$$

with $\mathbf{MLP}_{\text{enc}} : \mathbb{R}^{|\mathcal{V}^{n_\ell-1}| N_F^{n_\ell-1}} \times \mathbb{R}^{M \times |\mathcal{V}^{n_\ell-1}| N_F^{n_\ell-1}} \times \mathbb{R}^M \rightarrow \mathbb{R}^M$, where $\mathbf{W}^{n_\ell} \in \mathbb{R}^{M \times |\mathcal{V}^{n_\ell-1}| N_F^{n_\ell-1}}$ and $\mathbf{b}^{n_\ell} \in \mathbb{R}^M$ denote the weights and biases, respectively, with $\Theta_{n_\ell} = \{\mathbf{W}^{n_\ell}, \mathbf{b}^{n_\ell}\}$. The final layer of the encoder architecture takes the form

$$\mathbf{h}_{n_\ell} : (\mathbf{X}^{n_\ell-1}; \Theta_{n_\ell}) \mapsto \mathbf{MLP}_{\text{enc}}(\cdot; \Theta_{n_\ell}) \circ \mathbf{Flatten}(\mathbf{X}^{n_\ell-1}), \quad (15)$$

with $\mathbf{h}_{n_\ell} : \mathbb{R}^{|\mathcal{V}^{n_\ell-1}| \times N_F^{n_\ell-1}} \times \mathbb{R}^{M \times |\mathcal{V}^{n_\ell-1}| N_F^{n_\ell-1}} \times \mathbb{R}^M \rightarrow \mathbb{R}^M$. The output of this layer, $\hat{\mathbf{x}} \in \mathbb{R}^M$, is the low-dimensional latent representation of the solution state.

3.3. Decoder architecture

Much like the encoder, the decoder architecture deploys the hierarchy of reduced graphs from Section 3.1. The decoder consists of layers $i = 0, \dots, n_\ell$. The zeroth layer ($i = 0$), outlined in Section 3.3.1, utilizes an MLP to reconstruct a small graph from the low-dimensional latent representation, $\hat{\mathbf{x}}$. Layers $i = 1, \dots, n_\ell - 1$, outlined in Section 3.3.2, leverage the hierarchy of reduced graphs from Section 3.1 in reverse order to perform unpooling and message passing (UMP) to increase the dimension of the system. The final layer of the decoder ($i = n_\ell$), outlined in section 3.3.3, is a postprocessing layer that restructures the output graph into a state vector for deployment in the time integration scheme.

3.3.1. Fully-connected layer: expansion – Layer 0

The zeroth layer of the decoder ($i = 0$) entails two functions. It first applies a fully-connected/MLP layer to the latent representation,

$$\mathbf{MLP}_{\text{dec}} : (\hat{\mathbf{x}}; \Omega_0) \mapsto \sigma(\mathcal{W}^0 \hat{\mathbf{x}} + \boldsymbol{\beta}^0), \quad (16)$$

with $\mathbf{MLP}_{\text{dec}} : \mathbb{R}^M \times \mathbb{R}^{|\mathcal{V}^{n_\ell-1}| N_F^{n_\ell-1} \times M} \times \mathbb{R}^{|\mathcal{V}^{n_\ell-1}| N_F^{n_\ell-1}} \rightarrow \mathbb{R}^{|\mathcal{V}^{n_\ell-1}| N_F^{n_\ell-1}}$, where $\mathcal{W}^0 \in \mathbb{R}^{|\mathcal{V}^{n_\ell-1}| N_F^{n_\ell-1} \times M}$ and $\boldsymbol{\beta}^0 \in \mathbb{R}^{|\mathcal{V}^{n_\ell-1}| N_F^{n_\ell-1}}$ denote the weights and biases of the MLP layer of the decoder, respectively, with $\Omega_0 = \{\mathcal{W}^0, \boldsymbol{\beta}^0\}$, and $\sigma : \mathbb{R} \rightarrow \mathbb{R}$ denotes the element-wise activation function, chosen here to be the ELU activation function [65]. An unflattening operator is then applied to the output of the fully-connected layer, $\bar{\mathbf{y}}^0$, to generate a node feature matrix corresponding to the $n_\ell - 1$ graph in the hierarchy of reduced graphs, **Unflatten** : $\bar{\mathbf{y}}^0 \mapsto \mathbf{Y}^0$, with **Unflatten** : $\mathbb{R}^{|\mathcal{V}^{n_\ell-1}| N_F^{n_\ell-1}} \rightarrow \mathbb{R}^{|\mathcal{V}^{n_\ell-1}| \times N_F^{n_\ell-1}}$, where $\bar{\mathbf{y}}^0 \in \mathbb{R}^{|\mathcal{V}^{n_\ell-1}| N_F^{n_\ell-1}}$ denotes the output of $\mathbf{MLP}_{\text{dec}}$ and $\mathbf{Y}^0 \in \mathbb{R}^{|\mathcal{V}^{n_\ell-1}| \times N_F^{n_\ell-1}}$. We note that the unflattening operator is similar to the **Matricize** operator introduced previously but applied to a vector with a size different from the full-order state vector. Ultimately, the first layer of the decoder takes the form

$$\mathbf{g}_0 : (\hat{\mathbf{x}}; \Omega_0) \mapsto \mathbf{Unflatten}(\cdot) \circ \mathbf{MLP}_{\text{dec}}(\hat{\mathbf{x}}; \Omega_0), \quad (17)$$

where $\mathbf{g}_0 : \mathbb{R}^M \times \mathbb{R}^{|\mathcal{V}^{n_\ell-1}| N_F^{n_\ell-1} \times M} \times \mathbb{R}^{|\mathcal{V}^{n_\ell-1}| N_F^{n_\ell-1}} \rightarrow \mathbb{R}^{|\mathcal{V}^{n_\ell-1}| \times N_F^{n_\ell-1}}$.

3.3.2. Unpooling and message passing (UMP) – Layers $1, \dots, n_\ell - 1$

The next layers in the decoder architecture ($i = 1, \dots, n_\ell - 1$) consist of UMP layers. The first step in a UMP layer is to perform an unpooling operation, wherein nodes are reintroduced to the graph, and their feature vectors are interpolated. In layer i of the decoder with $i = 1, \dots, n_\ell - 1$, the unpooling operation receives a graph of layer $n_\ell - i$ as an input and outputs a graph of layer $n_\ell - i - 1$ in the hierarchy of $n_\ell - 1$ graphs of the encoder. For example in Figure 4 with $n_\ell = 3$, the input and output to the second layer of the decoder ($i = 2$) are the graphs of 1st layer ($n_\ell - i = 1$)

and the zeroth layer ($n_\ell - i - 1 = 0$) of the hierarchy of graphs in the encoder, respectively. For ease of notation, we introduce $\hat{i} = n_\ell - i$ as a counter used to denote the hierarchy of reduced graphs in the opposite order as the encoder. In the unpooling operation of layer i of the decoder, a node's features of graph \hat{i} are interpolated using the k -nearest neighbors of the node features of graph $\hat{i} - 1$,

$$\mathbf{Unpool}^i : \mathbf{Y}^{i-1} \mapsto \frac{\sum_{n \in \mathcal{N}^{\hat{i}-1}(j)} \mathbf{w}(\mathbf{Pos}_j^{\hat{i}-1}, \mathbf{Pos}_n^{\hat{i}}) \mathbf{Y}_n^{i-1}}{\sum_{n \in \mathcal{N}^{\hat{i}-1}(j)} \mathbf{w}(\mathbf{Pos}_j^{\hat{i}-1}, \mathbf{Pos}_n^{\hat{i}})}, \quad j = 1, \dots, |\mathcal{V}^{\hat{i}-1}| \quad (18)$$

where,

$$\mathbf{w} : (\mathbf{Pos}_j^{\hat{i}-1}, \mathbf{Pos}_n^{\hat{i}}) \mapsto \frac{1}{\|\mathbf{Pos}_j^{\hat{i}-1} - \mathbf{Pos}_n^{\hat{i}}\|}, \quad (19)$$

with $\mathbf{Unpool}^i : \mathbb{R}^{|\mathcal{V}^{\hat{i}}| \times N_F^{\hat{i}}} \rightarrow \mathbb{R}^{|\mathcal{V}^{\hat{i}-1}| \times N_F^{\hat{i}}}$, $\mathcal{N}^{\hat{i}-1}(j)$ is the k -nearest neighbors in $\mathcal{V}^{\hat{i}}$ of the j^{th} node in $\mathcal{V}^{\hat{i}-1}$, with $k \in \mathbb{N}$ denoting the number of nearest neighbors used for interpolation. $\mathbf{Pos}_j^{\hat{i}-1} \in \mathbb{R}^{n_d}$ is the spatial position of the j^{th} node at the $(\hat{i} - 1)^{\text{th}}$ layer of the hierarchy of reduced graphs, $\mathbf{Pos}_n^{\hat{i}} \in \mathbb{R}^{n_d}$ is the spatial position of the n^{th} node in the \hat{i}^{th} layer in the hierarchy of reduced graphs, $\mathbf{w} : \mathbb{R}^{n_d} \times \mathbb{R}^{n_d} \rightarrow \mathbb{R}_+$ denotes the spatial interpolation function, and $\|\cdot\| : \mathbb{R}^{n_d} \rightarrow \mathbb{R}_+$ denotes the Euclidean norm. Much like the SAGEConv function (11), the unpooling of (18) is performed by looping over all nodes, $j \in \mathcal{V}^{\hat{i}-1}$, to compute the rows $j = 1, \dots, |\mathcal{V}^{\hat{i}-1}|$ of the output of the unpooling operation, $\bar{\mathbf{Y}}^{i-1} \in \mathbb{R}^{|\mathcal{V}^{\hat{i}-1}| \times N_F^{\hat{i}}}$.

Next, a message passing operation is applied to the outputs of the unpooling operation,

$$\mathbf{MP}_{\text{dec}}^i : (\bar{\mathbf{Y}}^{i-1}; \mathbf{\Omega}_i) \mapsto \sigma(\bar{\mathbf{Y}}_j^{i-1} \mathbf{W}_1^i + (\text{mean}_{n \in \mathcal{K}^{\hat{i}-1}(j)} \bar{\mathbf{Y}}_n^{i-1}) \mathbf{W}_2^i), \quad j = 1, \dots, |\mathcal{V}^{\hat{i}-1}|, \quad (20)$$

with $\mathbf{MP}_{\text{dec}}^i : \mathbb{R}^{|\mathcal{V}^{\hat{i}-1}| \times N_F^{\hat{i}}} \times \mathbb{R}^{N_F^{\hat{i}} \times N_F^{\hat{i}-1}} \times \mathbb{R}^{N_F^{\hat{i}} \times N_F^{\hat{i}-1}} \rightarrow \mathbb{R}^{|\mathcal{V}^{\hat{i}-1}| \times N_F^{\hat{i}-1}}$, where $\mathbf{W}_1^i, \mathbf{W}_2^i \in \mathbb{R}^{N_F^{\hat{i}} \times N_F^{\hat{i}-1}}$ denote the weights with $\mathbf{\Omega}_i = \{\mathbf{W}_1^i, \mathbf{W}_2^i\}$ denoting the set of weights for the i^{th} UMP layer, $\mathcal{K}^{\hat{i}-1}(j)$ denotes the set of nodes connected to node j in the graph of $(\hat{i} - 1)^{\text{th}}$ layer based on the adjacency matrix $\mathbf{A}^{\hat{i}-1}$, where the subscripts j and n denote the j^{th} and n^{th} nodes, respectively, and $\sigma : \mathbb{R} \rightarrow \mathbb{R}$ denotes the element-wise activation function, chosen here to be the ELU activation function [65]. According to (20), the output of $\mathbf{MP}_{\text{dec}}^i$ is determined in a row-wise manner.

Ultimately, the UMP layer takes the form,

$$\mathbf{g}_i : (\mathbf{Y}^{i-1}; \mathbf{\Omega}_i) \mapsto \mathbf{MP}_{\text{dec}}^i(\cdot; \mathbf{\Omega}_i) \circ \mathbf{Unpool}^i(\mathbf{Y}^{i-1}), \quad (21)$$

with $\mathbf{g}_i : \mathbb{R}^{|\mathcal{V}^{\hat{i}}| \times N_F^{\hat{i}}} \times \mathbb{R}^{N_F^{\hat{i}} \times N_F^{\hat{i}-1}} \times \mathbb{R}^{N_F^{\hat{i}} \times N_F^{\hat{i}-1}} \rightarrow \mathbb{R}^{|\mathcal{V}^{\hat{i}-1}| \times N_F^{\hat{i}-1}}$. Hence, the UMP layer increases the number of nodes in a given graph and decreases the number of features associated with each node, and it gives the node feature matrix \mathbf{Y}^i as the output. The UMP layer is visually represented in Figure 7.

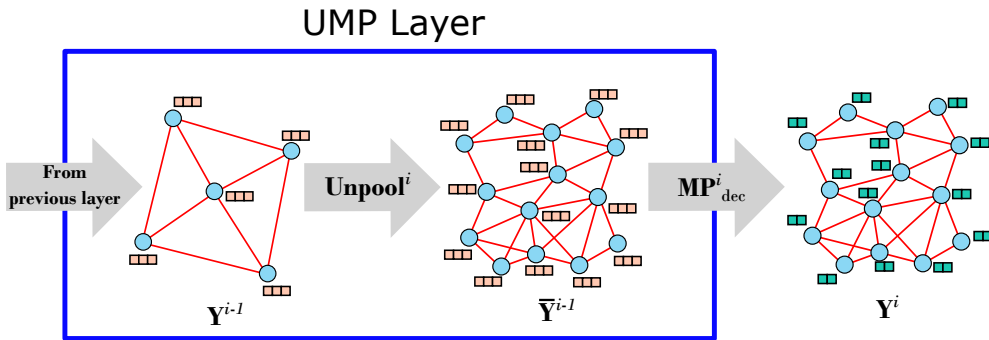


Figure 7: UMP layer used in the decoder of our graph autoencoder. The layer accepts a graph as an input and performs an unpooling operation to re-introduce nodes into the graph, thus increasing the dimension of the graph. Next, message passing is performed on the unpooled graph to exchange information between locally connected nodes.

3.3.3. Postprocessing – Layer n_ℓ

To represent the output of the decoder as a state vector for appropriate deployment in the time integration scheme, a postprocessing step is applied as the final layer ($i = n_\ell$). First, the **InvScale** operator is applied to invert the original **Scale** operation,

$$\mathbf{InvScale} : \mathbf{Y}_{ij}^{n_\ell-1} \mapsto \mathbf{Y}_{ij}^{n_\ell-1} (\mathcal{X}_j^{\max} - \mathcal{X}_j^{\min}) + \mathcal{X}_j^{\min}, \quad (22)$$

where $\mathbf{InvScale} : \mathbb{R} \rightarrow \mathbb{R}$ is an element-wise scaling operator. Next, a **Vectorize** operator is applied to reshape the output of the decoder to a state vector. Ultimately, the postprocessing step takes the form,

$$\mathbf{g}_{n_\ell} : (\mathbf{Y}^{n_\ell-1}; \mathbf{\Omega}_{n_\ell}) \mapsto \mathbf{Vectorize}(\cdot) \circ \mathbf{InvScale}(\mathbf{Y}^{n_\ell-1}), \quad (23)$$

where $\mathbf{g}_{n_\ell} : \mathbb{R}^{N_c \times n_q} \rightarrow \mathbb{R}^{N_c n_q}$, and $\mathbf{\Omega}_{n_\ell} = \emptyset$ is the empty set, as there are no trainable parameters in the postprocessing layer. The output of the decoder $\tilde{\mathbf{x}} \in \mathbb{R}^N$ is a reconstruction of the original state vector \mathbf{x} .

3.4. Training the autoencoder and regularization

The only components of the autoencoder that require training are the message passing operations and fully-connected/MLP layers with $\theta = \{\Theta_1, \Theta_2, \dots, \Theta_{n_\ell}\}$, $\omega = \{\Omega_0, \Omega_1, \dots, \Omega_{n_\ell-1}\}$ as trainable parameters. To train these, we adopt the same loss function as Lee and Carlberg [46, 47], which is the L^2 -norm of the reconstructed solution state,

$$\mathcal{L} = \sum_{i=1}^{N_{\text{train}}} \|\mathbf{x}^i - \mathbf{Dec}(\cdot) \circ \mathbf{Enc}(\mathbf{x}^i)\|_2^2, \quad (24)$$

where $\mathbf{x}^i \in \mathbb{R}^N$ is the i^{th} solution state in the training set and $N_{\text{train}} \in \mathbb{N}$ denotes the total number of solution states generated by the FOM.

As is common with neural ODEs [41, 66, 67], our decoder architecture was empirically noticed to be prone to generating an ill-conditioned system during time integration (the procedure of which is outlined in Section 4). As a remedy, we chose to adopt the regularization strategy from Josias and Brink [67], where a regularization term, taken to be the ratio of the maximum and minimum singular values of the Jacobian of the decoder, is added to (24) during training. Hence, our training minimizes:

$$\mathcal{L} = \sum_{i=1}^{N_{\text{train}}} \|\mathbf{x}^i - \mathbf{Dec}(\cdot) \circ \mathbf{Enc}(\mathbf{x}^i)\|_2^2 + \frac{\lambda}{N_{\text{train}}} \sum_{i=1}^{N_{\text{train}}} \left(\frac{\sigma_{\max}^i}{\sigma_{\min}^i} - 1 \right)^2, \quad (25)$$

where $\lambda \in \mathbb{R}$ is a user-prescribed regularization parameter, and $\sigma_{\max}^i \in \mathbb{R}$ and $\sigma_{\min}^i \in \mathbb{R}$ denote the maximum and minimum singular values of the Jacobian of the decoder, respectively, of the i^{th} solution state in the training set.

4. Time integration

In the literature, time stepping for ROMs using autoencoders has been achieved by a variety of methods, including training neural networks to compute time updates [36, 37, 38, 68, 69] and projecting the governing equations of the FOM onto a nonlinear manifold [46, 47, 54]. For GD-LSPG, we adopt a similar strategy to that of Lee and Carlberg [46], due to its ability to perform time-discrete residual minimization. GD-LSPG leverages the graph autoencoder to project the governing equations onto a low-dimensional latent space, thus performing time integration on the latent state variable. To illustrate, we set the initial conditions of the low-dimensional state vector to be the encoding of the initial conditions of the high-dimensional system, i.e., $\hat{\mathbf{x}}(0; \boldsymbol{\mu}) = \mathbf{Enc}(\mathbf{x}(0; \boldsymbol{\mu}))$, and approximate the full-order state vector of the solution of the system, (1), to be,

$$\tilde{\mathbf{x}}(t; \boldsymbol{\mu}) \approx \mathbf{Dec}(\hat{\mathbf{x}}(t; \boldsymbol{\mu})), \quad (26)$$

where $\tilde{\mathbf{x}} : \mathbb{R}_+ \times \mathcal{D} \rightarrow \mathbb{R}^N$ denotes the predicted solution state. Next, we substitute (26) into (3) to obtain the following minimization problem:

$$\hat{\mathbf{x}}(t; \boldsymbol{\mu}) = \operatorname{argmin}_{\hat{\boldsymbol{\xi}} \in \mathbb{R}^M} \|\mathbf{r}(\mathbf{Dec}(\hat{\boldsymbol{\xi}}(t; \boldsymbol{\mu})))\|_2^2, \quad (27)$$

where $\hat{\xi} \in \mathbb{R}^M$ is the sought-after low-dimensional solution state at time t . Numerically obtaining this solution is well-studied in the literature [25, 26, 46, 47, 70], and is obtained by an iterative solver. At each iteration of time step n , the update

$$\hat{\mathbf{x}}^{n(j+1)} = \hat{\mathbf{x}}^{n(j)} - \beta^{(j)} \left(\left(\Psi(\hat{\mathbf{x}}^{n(j)}; \mu) \right)^T \Psi(\hat{\mathbf{x}}^{n(j)}; \mu) \right)^{-1} \left(\Psi(\hat{\mathbf{x}}^{n(j)}; \mu) \right)^T \mathbf{r}(\text{Dec}(\hat{\mathbf{x}}^{n(j)}); \mu), \quad (28)$$

is performed, where the superscript $n(j)$ denotes the j^{th} iteration of n^{th} time step, $\beta^{(j)} \in \mathbb{R}_+$ is the step size chosen to satisfy Wolfe conditions [71], and the test basis matrix, $\Psi : \mathbb{R}^M \times \mathcal{D} \rightarrow \mathbb{R}^{N \times M}$, is defined to be:

$$\Psi : (\hat{\xi}; \mu) \mapsto \left(\frac{\partial \mathbf{r}}{\partial \mathbf{x}} \Big|_{\text{Dec}(\hat{\xi}(t; \mu))} \right) \left(\frac{d \text{Dec}}{d \hat{\xi}} \Big|_{\hat{\xi}(t; \mu)} \right). \quad (29)$$

An initial guess at each time step is chosen to be $\hat{\mathbf{x}}^{n(0)} = \hat{\mathbf{x}}^{n-1}$, where $\hat{\mathbf{x}}^{n-1}$ denotes the converged solution from the previous time step, $n - 1$. The solution is updated iteratively until the L^2 -norm of the reduced-state residual for the current iteration falls below a user-prescribed fraction of that of the initial guess at the time step $n = 1$ (which is equal to the initial condition), where $\kappa \in [0, 1]$ is the user-defined tolerance,

$$\text{Convergence criterion} : \frac{\left\| \hat{\mathbf{r}}(\hat{\mathbf{x}}^{n(j)}; \mu) \right\|_2}{\left\| \hat{\mathbf{r}}(\hat{\mathbf{x}}^0; \mu) \right\|_2} \leq \kappa, \quad (30)$$

where the reduced state residual $\hat{\mathbf{r}}$ is obtained from the projection of the residual,

$$\hat{\mathbf{r}} : (\hat{\xi}; \mu) \mapsto \left(\Psi(\hat{\xi}; \mu) \right)^T \mathbf{r}(\text{Dec}(\hat{\xi}); \mu). \quad (31)$$

5. Numerical experiments

To evaluate the efficiency and accuracy of the GD-LSPG method, we employ two test problems. First, to provide a baseline for comparison to the rest of the literature, we use a commonly studied 1D Burgers' equation model using a structured mesh [46, 47, 72, 73]. This allows us to benchmark the accuracy of GD-LSPG with PMOR methods that deploy CNN-based autoencoders. Second, we deploy GD-LSPG to a model for the 2D Euler equations using an unstructured mesh resulting in a Riemann Problem [74, 75] to demonstrate GD-LSPG's ability to extend to unstructured meshes where CNN-based autoencoders have been inapplicable. All autoencoders are trained with PyTorch [76] and PyTorch-Geometric [77]. A detailed description of the employed autoencoder architectures and choice of hyperparameters for both examples are provided in Appendix A. To train the models and therefore minimize (25), the Adam optimizer [78] is deployed to perform stochastic gradient descent with an adaptive learning rate. In this section, we use three performance metrics to assess accuracy. First, reconstruction error is used to assess the autoencoder's ability to encode and decode a precomputed solution,

$$\text{Autoencoder reconstruction error} = \frac{\sqrt{\sum_{n=1}^{N_t} \left\| \mathbf{x}^n(\mu) - \text{Dec} \circ \text{Enc}(\mathbf{x}^n(\mu)) \right\|_2^2}}{\sqrt{\sum_{n=1}^{N_t} \left\| \mathbf{x}^n(\mu) \right\|_2^2}}, \quad (32)$$

where $\mathbf{x}^n(\mu)$ is the full-order solution at the n^{th} time step. Second, the POD reconstruction error is used to assess an affine latent space's ability to project and reconstruct a precomputed solution,

$$\text{POD reconstruction error} = \frac{\sqrt{\sum_{n=1}^{N_t} \left\| (\mathbf{I} - \Phi \Phi^T) \mathbf{x}^n(\mu) \right\|_2^2}}{\sqrt{\sum_{n=1}^{N_t} \left\| \mathbf{x}^n(\mu) \right\|_2^2}}, \quad (33)$$

where $\Phi \in \mathbb{R}^{N \times M}$ is the matrix of reduced basis vectors from an affine POD approximation constructed based on the method of snapshots (see Appendix B). Finally, the state prediction error is used to assess the accuracy of the ROM obtained from different methods in predicting the full-order solution,

$$\text{State prediction error} = \frac{\sqrt{\sum_{n=1}^{N_t} \|\mathbf{x}^n(\boldsymbol{\mu}) - \tilde{\mathbf{x}}^n(\boldsymbol{\mu})\|_2^2}}{\sqrt{\sum_{n=1}^{N_t} \|\mathbf{x}^n(\boldsymbol{\mu})\|_2^2}}. \quad (34)$$

5.1. One-dimensional Burgers' equation

Using the same numerical experiment as Rewieński [73] and Lee and Carlberg [46, 47], we benchmark GD-LSPG's ability to perform PMOR upon an advection-driven problem. The governing equation for the 1D inviscid Burgers' equation, a common benchmark problem for shock propagation, is as follows.

$$\begin{aligned} \frac{\partial w(x, t; \boldsymbol{\mu})}{\partial t} + \frac{\partial f(w(x, t; \boldsymbol{\mu}))}{\partial x} &= 0.02e^{\mu_2 x}, \quad \forall x \in (0, L), \forall t \in (0, T] \\ w(0, t; \boldsymbol{\mu}) &= \mu_1, \quad \forall t \in (0, T] \\ w(x, 0; \boldsymbol{\mu}) &= 1, \quad \forall x \in (0, L), \end{aligned} \quad (35)$$

where $f(w) = 0.5w^2$, $x \in \mathbb{R}$ denotes spatial position, $t \in \mathbb{R}_+$ denotes time, $L \in \mathbb{R}$ denotes the length of the 1D physical domain, and $T \in \mathbb{R}_+$ denotes the final time. The finite volume method is deployed by dividing the spatial domain into 256 equally-sized cells over a domain of length $L = 100$, lending to a structured finite volume mesh. A backward-Euler time-integration scheme is employed, which corresponds to the cell-wise equations at the i^{th} cell,

$$p_i : (\boldsymbol{\xi}, t; \boldsymbol{\mu}, \Delta t) \mapsto \frac{\Delta t}{2\Delta x} \left((w_i^{n+1})^2 - (w_{i-1}^{n+1})^2 \right) - 0.02e^{\mu_2 x_i}, \quad (36)$$

with $q_i = 0$, $k = 1$, $\alpha_0 = 1$, and $\alpha_1 = -1$ when rearranged in the form of (2). Note that since Burgers' equation involves only one state variable, i.e., \mathbf{p}_i and \mathbf{q}_i are scalar variables. In (36), $\Delta x \in \mathbb{R}_+$ is the length of each cell in the uniform 1D mesh, $x_i \in \mathbb{R}$ is the coordinate of the center of the i^{th} cell in the mesh, and $\boldsymbol{\xi} = (w_1^{n+1}, w_2^{n+1}, \dots, w_{N_c}^{n+1})^T$ is the sought-after state solution at the $(n+1)^{\text{th}}$ time step. The time integration scheme uses a constant time step size $\Delta t = .07$ and a final time $T = 35$ for a total of 501 time steps per solution including the initial value. To train both the CNN-based autoencoder and the graph autoencoder, as well as obtain an affine POD basis, the solution to the FOM is computed for a total of 80 parameter scenarios with the parameters $\boldsymbol{\mu} = (\mu_1 = 4.25 + (\frac{1.25}{9})i, \mu_2 = .015 + (\frac{0.15}{7})j)$, for $i = 0, \dots, 9$ and $j = 0, \dots, 7$. Once trained, the autoencoders are deployed in an online setting to perform time integration for their respective ROMs. The Jacobian of the decoder is approximated using a finite difference scheme at both the offline training stage and the online prediction stage (refer to Appendix A for further details).

Empirically, we find that setting the user-defined tolerance, i.e., κ in (30), to be 10^{-3} for GD-LSPG and dLSPG, and 10^{-4} for POD-LSPG to be sufficient to achieve dependably accurate and converging solutions. For GD-LSPG, we employ an adaptive step size that starts at $\beta^{(0)} = 0.75$ for each time step and reduces by 5% every 10 iterations. Similarly for dLSPG, at each time step, we begin with $\beta^{(0)} = 1.0$ and reduce by 5% every 10 iterations. For POD-LSPG, we simply take $\beta^{(j)} = 1.0$ for all iterations.

Figure 8 depicts the solution state at various time steps for two test parameter set realizations not seen in the training set and two latent space dimensions of $M = 5, 10$. Additionally, the POD reconstruction errors from (33), and autoencoder reconstruction errors from (32) for the CNN-based autoencoder, inspired by [46, 47], and the reconstruction errors from the graph autoencoder can be found in Figure 8. Using the state prediction error of (34), we compare GD-LSPG to the traditional affine POD-based least-squares Petrov-Galerkin (POD-LSPG) projection [25, 70], as well as dLSPG, which leverages a CNN-based autoencoder [46, 47].

We emphasize that the reconstruction errors for the graph autoencoder are more than an order of magnitude smaller than that of the affine POD approximation for latent space dimensions 3 to 10. Likewise, the state prediction errors of GD-LSPG are roughly an order of magnitude lower than that of POD-LSPG for latent space dimensions 4 to 10. This outcome is due to the fact that an affine subspace is not well-suited for such nonlinear problems. Benchmarking the graph autoencoder with the traditional CNN-based autoencoder, we find that the graph autoencoder's reconstruction errors and state prediction errors to be less than an order of magnitude greater than those of the CNN-based autoencoder for the vast majority of latent space dimensions. This comparison implies that, while GD-LSPG

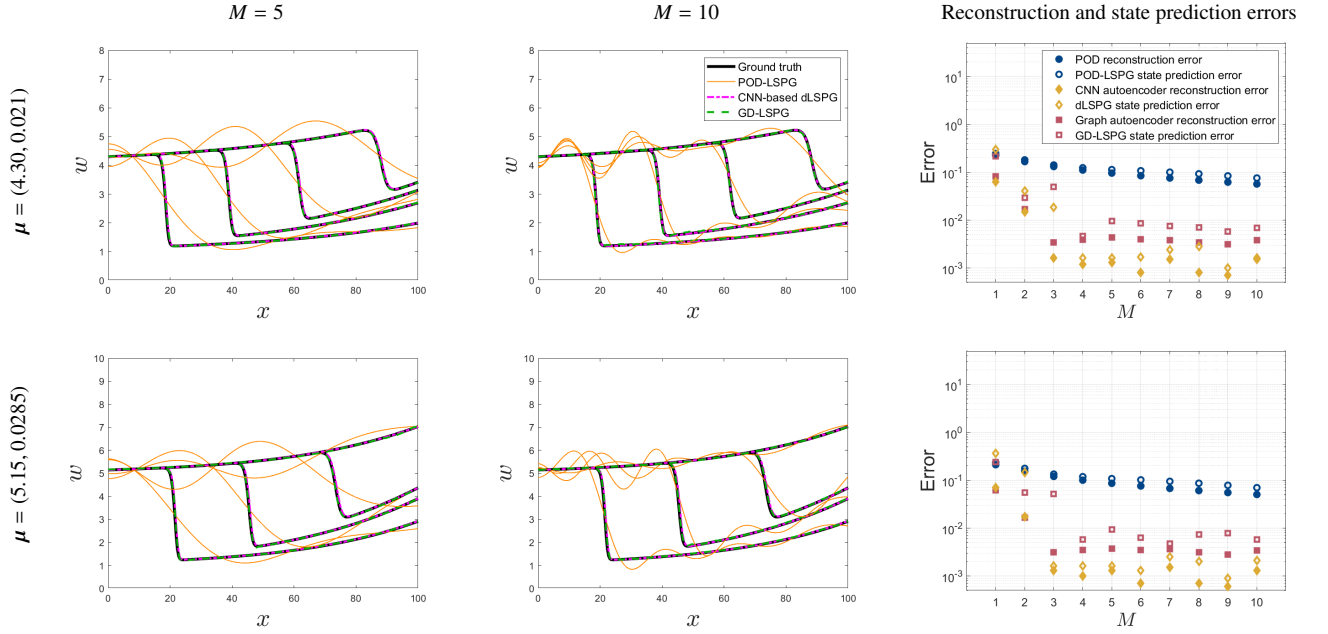


Figure 8: The left two columns represent the state solution for Burgers' equation (35) at several time steps for two latent space dimensions ($M = 5, 10$, respectively), while the right column depicts the error metrics for various PMOR methods. Figures in the first row correspond to test parameters $\boldsymbol{\mu} = (\mu_1 = 4.30, \mu_2 = 0.021)$, while figures in the second row correspond to test parameters $\boldsymbol{\mu} = (\mu_1 = 5.15, \mu_2 = 0.0285)$. GD-LSPG and dLSPG both outperform POD-LSPG in predicting the highly nonlinear behavior of the Burgers' equation. (Online version in color.)

gains adaptability and is applicable to unstructured meshes, it does not perform as well as CNN-based dLSPG for the Burgers' equation with a structured mesh. Still, we emphasize that, qualitatively, GD-LSPG is able to model the advection-dominated shock behavior in a manner similar to traditional CNN-based dLSPG, where traditional affine POD-LSPG tends to fail. Figure 9 depicts the difference between the ROM prediction of the full-order state vector and the FOM results with space and time. It can be seen that both dLSPG and GD-LSPG provide an improved ability to model the shock behavior of (35) over POD-LSPG. Additionally, it is apparent that the main source of error for GD-LSPG is a slight phase lag between the ground truth location of the shock and GD-LSPG's prediction of the shock location. Hence, on a structured mesh, GD-LSPG provides an improvement over traditional affine POD-LSPG [25, 26] in a manner comparable to that of dLSPG [46, 47, 48].

To assess the computational cost of the GD-LSPG method and compare it to POD-LSPG and dLSPG, we provide an analysis of the 1D Burgers' equation model. We found the online ROMs to be much more stable when deployed on a central processing unit (CPU) as opposed to a graphics processing unit (GPU). We believe this to be due to the numerical roundoff error introduced in the finite difference Jacobian, but leave it as an area of future investigation. As a result, all operations in this section are performed in PyTorch using a single Intel(R) Xeon(R) Platinum 8358 CPU @ 2.60GHz ICE LAKE core. Figure 10 reports the times associated with various components of the time integration procedure. We present the time to get $\mathbf{r}^{n(k)}$ from (2) and evaluate its Jacobian, time to get the Jacobian of the decoder, time to check the convergence criterion (30)-(31), time to decode to the high-dimensional space (26), the time to compute Ψ , $\Psi^T \Psi$, and $\Psi^T \mathbf{r}^{n(k)}$, and time to update the low-dimensional solution state (28). We emphasize that none of these methods employ a hyper-reduction scheme. Consequently, none of them achieve cost-savings with respect to the FOM.

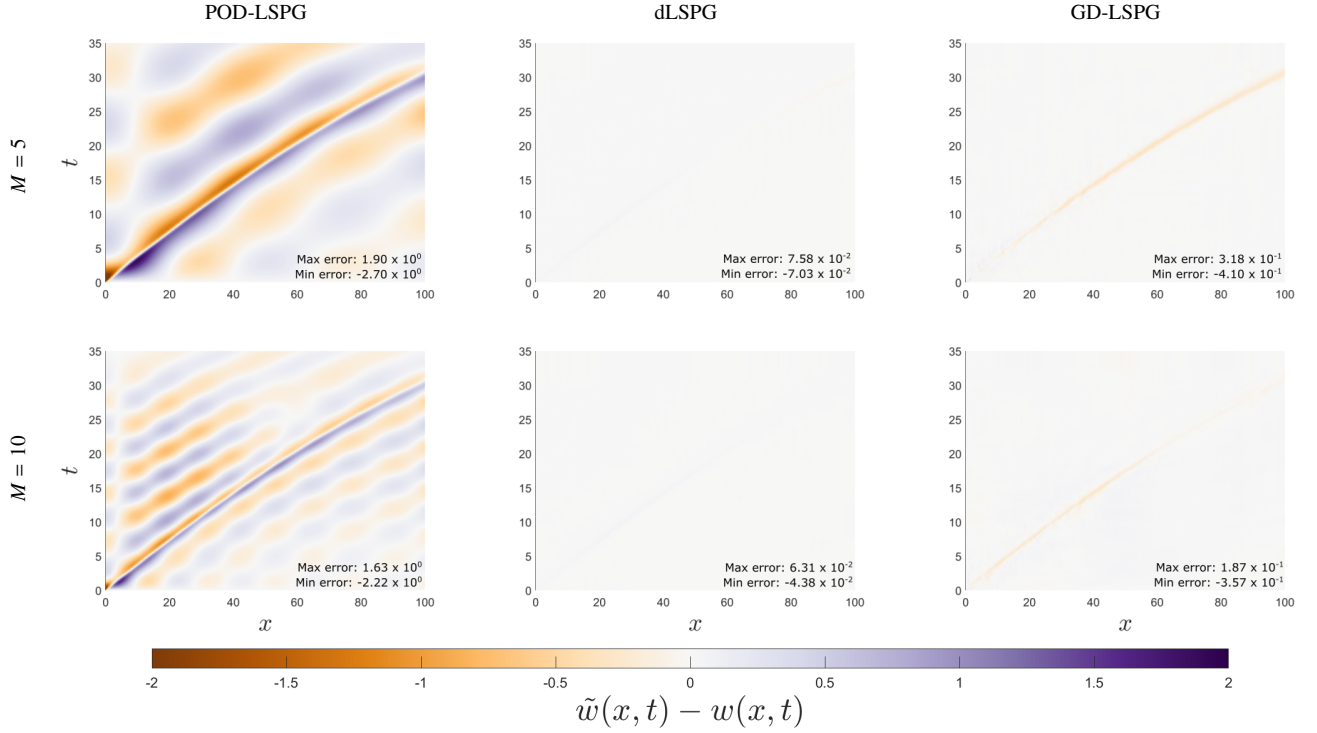


Figure 9: Local error for dLSPG, GD-LSPG, and POD-LSPG for the parameter set $\mu = (\mu_1 = 4.30, \mu_2 = 0.021)$. The top and bottom rows correspond to solutions generated with latent space dimensions $M = 5$ and $M = 10$, respectively. The local error is simply taken to be $\tilde{w}(x, t) - w(x, t)$, or the difference between the predicted solution state and the ground truth solution state. The POD-LSPG solution introduces considerable error throughout the domain. Alternatively, dLSPG and GD-LSPG introduce some lower-order localized errors, primarily around the shock. The slight phase difference between shocks in the predicted solution and the ground truth solution is the main error contributor. (Online version in color.)

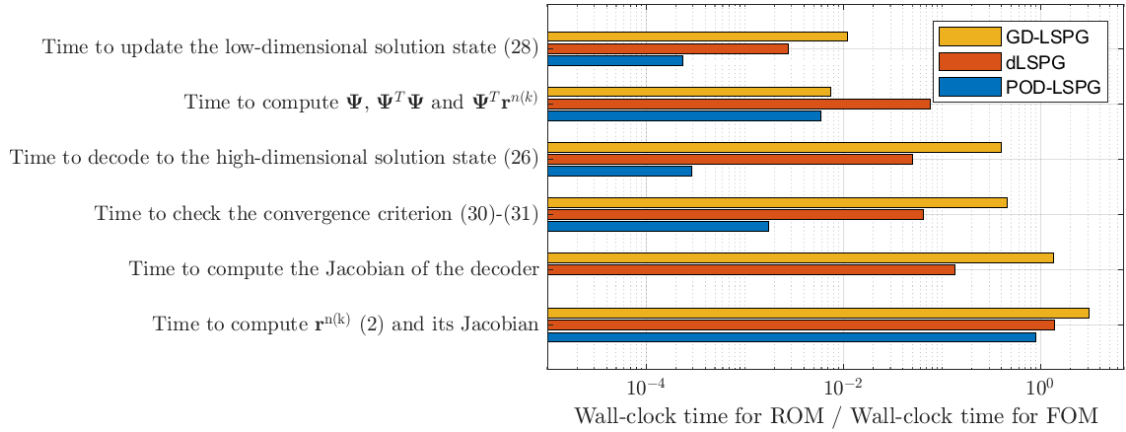


Figure 10: Wall-clock time breakdown of individual components of GD-LSPG, dLSPG, and POD-LSPG with a latent space dimension $M = 5$ normalized to the wall-clock time associated with the FOM solution. Solutions were generated for the parameter set $\mu = (\mu_1 = 4.30, \mu_2 = 0.021)$. The POD-LSPG approach does not have to compute the Jacobian of the decoder at each time step. The breakdown reveals the most expensive components of the dLSPG and GD-LSPG methods include the time to get the high-dimensional residual, Jacobian of the high-dimensional residual, and Jacobian of the decoder, all of which should have significantly reduced computational cost with the implementation of a hyper-reduction scheme. (Online version in color.)

5.2. Two-dimensional Euler equations with unstructured mesh resulting in a Riemann problem

In our second numerical experiment, we consider the FVM using an unstructured mesh to solve the two-dimensional Euler equations. We provide a brief overview of the important concepts in this section but the reader may consult [79, 80, 81, 82] for further reading on Riemann solvers for the Euler equations. We begin with the two-dimensional Euler equations in the form of hyperbolic PDEs:

$$\frac{\partial \mathbf{U}}{\partial t} + \frac{\partial \mathbf{F}}{\partial x} + \frac{\partial \mathbf{G}}{\partial y} = \mathbf{0}, \quad (37)$$

$$\mathbf{U} = \begin{bmatrix} \rho \\ \rho u \\ \rho v \\ \rho E \end{bmatrix}, \quad \mathbf{F} = \begin{bmatrix} \rho u \\ \rho u^2 + P \\ \rho uv \\ \rho u H \end{bmatrix}, \quad \mathbf{G} = \begin{bmatrix} \rho v \\ \rho uv \\ \rho v^2 + P \\ \rho v H \end{bmatrix}, \quad (38)$$

where $\rho \in \mathbb{R}_+$ denotes density, $u \in \mathbb{R}$ and $v \in \mathbb{R}$ denote velocities in the x and y directions, respectively, $P \in \mathbb{R}_+$ denotes pressure, $E = \frac{1}{\gamma-1} \frac{P}{\rho} + \frac{1}{2} (u^2 + v^2) \in \mathbb{R}_+$ and $H = \frac{\gamma}{\gamma-1} \frac{P}{\rho} + \frac{1}{2} (u^2 + v^2) \in \mathbb{R}_+$ denote specific total energy and enthalpy, respectively, and $\gamma \in \mathbb{R}_+$ is the specific heat ratio. We integrate (37) over a control volume, Γ , and apply the divergence theorem to get the form,

$$\int_{\Gamma} \frac{d}{dt} \mathbf{U} dV + \int_{\partial\Gamma} \mathbf{H} \cdot \hat{\mathbf{n}} dA = \mathbf{0}, \quad (39)$$

where $dA \in \mathbb{R}_+$ denotes the differential surface area of a control volume, $dV \in \mathbb{R}_+$ denotes the differential volume of a control volume, $\partial\Gamma$ denotes the surface of the control volume, $\mathbf{H} = \mathbf{F}\hat{\mathbf{i}} + \mathbf{G}\hat{\mathbf{j}}$, $\hat{\mathbf{n}} = n_x\hat{\mathbf{i}} + n_y\hat{\mathbf{j}}$ denotes the outward facing unit-normal vector from the control volume, where $\hat{\mathbf{i}}$ and $\hat{\mathbf{j}}$ denote the Cartesian unit vectors of x and y respectively, and $n_x \in [-1, 1]$ and $n_y \in [-1, 1]$ denote the components of $\hat{\mathbf{n}}$ decomposed in the x and y directions.

An approximate solution for (39) is obtained by first spatially discretizing the domain, where the surface integral term is approximated by obtaining the numerical flux passing over the cell faces in the unstructured mesh. The numerical flux is computed using a Riemann solver designed to resolve the computationally difficult nature of the hyperbolic Euler equations. In this numerical experiment, we choose a Rotated Roe, Harten, Lax, and van Leer (R-RHLL) flux from [79] coupled with a two-stage Runge-Kutta time integration scheme [83] to generate a time series solution. The resulting scheme for a single finite volume cell takes the form

$$\mathbf{U}_i^{n+1} = \mathbf{U}_i^n - \Delta t \sum_{j \in \mathcal{M}(i)} \Phi_{ij} \left(\mathbf{U}_i^n - \Delta t \sum_{j \in \mathcal{M}(i)} \Phi_{ij} (\mathbf{U}_i^n, \mathbf{U}_j^n), \mathbf{U}_j^n - \Delta t \sum_{k \in \mathcal{M}(j)} \Phi_{jk} (\mathbf{U}_j^n, \mathbf{U}_k^n) \right), \quad (40)$$

where $\mathbf{U}_i^n, \mathbf{U}_j^n, \mathbf{U}_k^n \in \mathbb{R}^4$ denote the state vector of the $i^{\text{th}}, j^{\text{th}},$ and k^{th} cells at the n^{th} time step, respectively, $\mathcal{M}(i)$ denotes the set of neighboring cells of the i^{th} cell (i.e., sharing an interface), $\Phi_{ij} : \mathbb{R}^4 \times \mathbb{R}^4 \rightarrow \mathbb{R}^4$ and $\Phi_{jk} : \mathbb{R}^4 \times \mathbb{R}^4 \rightarrow \mathbb{R}^4$ denote the functions that compute the R-RHLL flux at the interface between the $i^{\text{th}} - j^{\text{th}}$ and $j^{\text{th}} - k^{\text{th}}$ cells, respectively. Therefore, (40) can be written in the residual-minimization cell-wise form of (2) at the i^{th} cell with

$$\mathbf{q}_i : (\mathbf{U}^n, \mathbf{t}^n; \boldsymbol{\mu}, \Delta t) \mapsto \Delta t \sum_{j \in \mathcal{M}(i)} \Phi_{ij} \left(\mathbf{U}_i^n - \Delta t \sum_{j \in \mathcal{M}(i)} \Phi_{ij} (\mathbf{U}_i^n, \mathbf{U}_j^n), \mathbf{U}_j^n - \Delta t \sum_{k \in \mathcal{M}(j)} \Phi_{jk} (\mathbf{U}_j^n, \mathbf{U}_k^n) \right), \quad (41)$$

and $\mathbf{p}_i = \mathbf{0}$, $\alpha_0 = 1$, $\alpha_1 = -1$, $\tau = 1$, and $\boldsymbol{\xi} = (\mathbf{U}_1^{n+1}, \mathbf{U}_2^{n+1}, \dots, \mathbf{U}_{N_c}^{n+1})^T$. We note that the minimization problem associated with the residual of the FOM (40) is solved explicitly in the two-stage Runge-Kutta scheme. However, when the two-stage Runge-Kutta scheme is deployed in GD-LSPG, minimizing the projection of the residual onto the low-dimensional latent space according to (31) is performed implicitly using the iterative solver described in Section 4.

We solve (37)-(38) on the domain $x \in [0, 1]$, $y \in [0, 1]$ with inflow/outflow boundary conditions that are computed via the fluxes of the cells along each boundary. The initial conditions are defined by dividing the domain into quadrants, where a different state is defined in each quadrant (see Figure 11). In this experiment, we define the quadrants as a parameterized version of configuration G from [84] (or configuration 15 from [74, 75, 85]), i.e.,

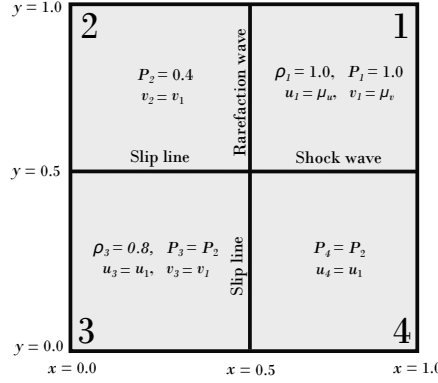


Figure 11: Setup for the parametric Euler equations to be solved by a Riemann solver with an unstructured finite volume mesh. The quadrants have been numbered in the figure. The problem's parameters are taken to be the initial x and y velocities in the top right quadrant, i.e., $\boldsymbol{\mu} = (\mu_u, \mu_v)$. Varying the initial velocity results in the shock wave and rarefaction wave propagating at different speeds and in different directions, resulting in an advection-driven flow.

$$\begin{aligned}
\rho_1 &= 1.0, & \rho_3 &= 0.8, \\
u_1 &= u_3 = u_4 = \mu_u, \\
v_1 &= v_2 = v_3 = \mu_v, \\
P_1 &= 1.0, & P_2 &= P_3 = P_4 = 0.4,
\end{aligned} \tag{42}$$

where $\mu_u, \mu_v \in \mathbb{R}$ are model's parameters, i.e., $\boldsymbol{\mu} = (\mu_u, \mu_v)$, and the remaining variables (ρ_2, ρ_4, u_2, v_4) are defined by the Rankine-Hugoniot relations and the relations for a polytropic gas. Specifically, the rarefaction wave yields the conditions,

$$\begin{aligned}
\rho_2 &= \rho_1 \left(\frac{P_2}{P_1} \right)^{\frac{1}{\gamma}}, \\
u_2 &= u_1 + \frac{2\sqrt{\gamma}}{\gamma-1} \left(\sqrt{\frac{P_2}{\rho_2}} - \sqrt{\frac{P_1}{\rho_1}} \right),
\end{aligned} \tag{43}$$

and the shock wave yields the conditions,

$$\begin{aligned}
\rho_4 &= \rho_1 \left(\frac{\frac{P_4}{P_1} + \frac{\gamma-1}{\gamma+1}}{1 + \frac{\gamma-1}{\gamma+1} \frac{P_4}{P_1}} \right), \\
v_4 &= v_1 + \sqrt{\frac{(P_4 - P_1)(\rho_4 - \rho_1)}{\rho_4 \rho_1}}.
\end{aligned} \tag{44}$$

Our model leverages Numba's just-in-time compiler [86] to compile the code efficiently. We generate an unstructured mesh with 4328 finite volume cells using Gmsh [87]. A sample solution with the deployed unstructured mesh is presented in Figure 12.

We perform a parametric study by varying the initial velocity in the top right quadrant via $\boldsymbol{\mu} = (\mu_u = -1.2 - 0.2i, \mu_v = -0.3 - 0.1j)$, with $i = 0, \dots, 4$ and $j = 0, \dots, 4$, resulting in solutions to 25 different parameter sets. We take $\Delta t = 0.001$ and $T_f = 0.3$, therefore collecting 301 snapshots for each parameter set including the initial conditions. The solutions from the parametric study were used as training data to train the autoencoder as outlined in Appendix A. For two test parameter sets not seen during training, $\boldsymbol{\mu} = (\mu_u = -1.3, \mu_v = -0.65)$ and $\boldsymbol{\mu} = (\mu_u = -1.9, \mu_v = -0.35)$, the solution states at $t = 0.15$ and $t = 0.3$ can be found in Figure 13. We approximate the Jacobian of the decoder using a finite difference scheme at both the offline training stage and online prediction stage (refer to Appendix A for further details). For POD-LSPG, we set the tolerance κ in (30) to be 10^{-4} and the step size $\beta^{(j)}$ to be 1.0 for all

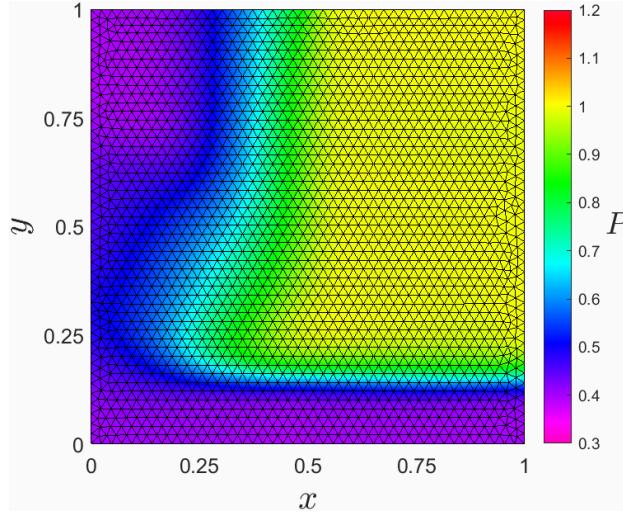


Figure 12: FOM solution to 2D Euler equations with parameter set $\mu = (\mu_u = -1.2, \mu_v = -0.3)$ at $t = 0.3$. We approximate a solution by spatially discretizing the physical domain with an unstructured finite volume mesh, which is not compatible with CNN-based autoencoders, and therefore necessitates GD-LSPG.

steps. For GD-LSPG, we set the tolerance κ in (30) to be 10^{-3} and employ an adaptive step size scheme with $\beta^{(0)}$ to be 1.0 reducing by 10% every 10 iterations. Like before, we compare POD projection errors from (33) with the autoencoder reconstruction error from (32) in Figure 14. Additionally, Figure 14 compares the state prediction error of POD-LSPG to GD-LSPG (obtained from (34) for both) with a varying dimension of the low-dimensional latent space, while Figure 15 presents the local error of several solution states generated by POD-LSPG and GD-LSPG. Again, we note that both qualitatively and quantitatively, the graph autoencoder and its deployment in GD-LSPG is more accurately able to model the moving rarefaction waves, shock waves, and contact waves than the affine POD projection and POD-LSPG. The traditional POD-LSPG solutions are far more diffusive than the solution to the FOM and, as a result, fail to model the advection-driven behavior present in this solution.

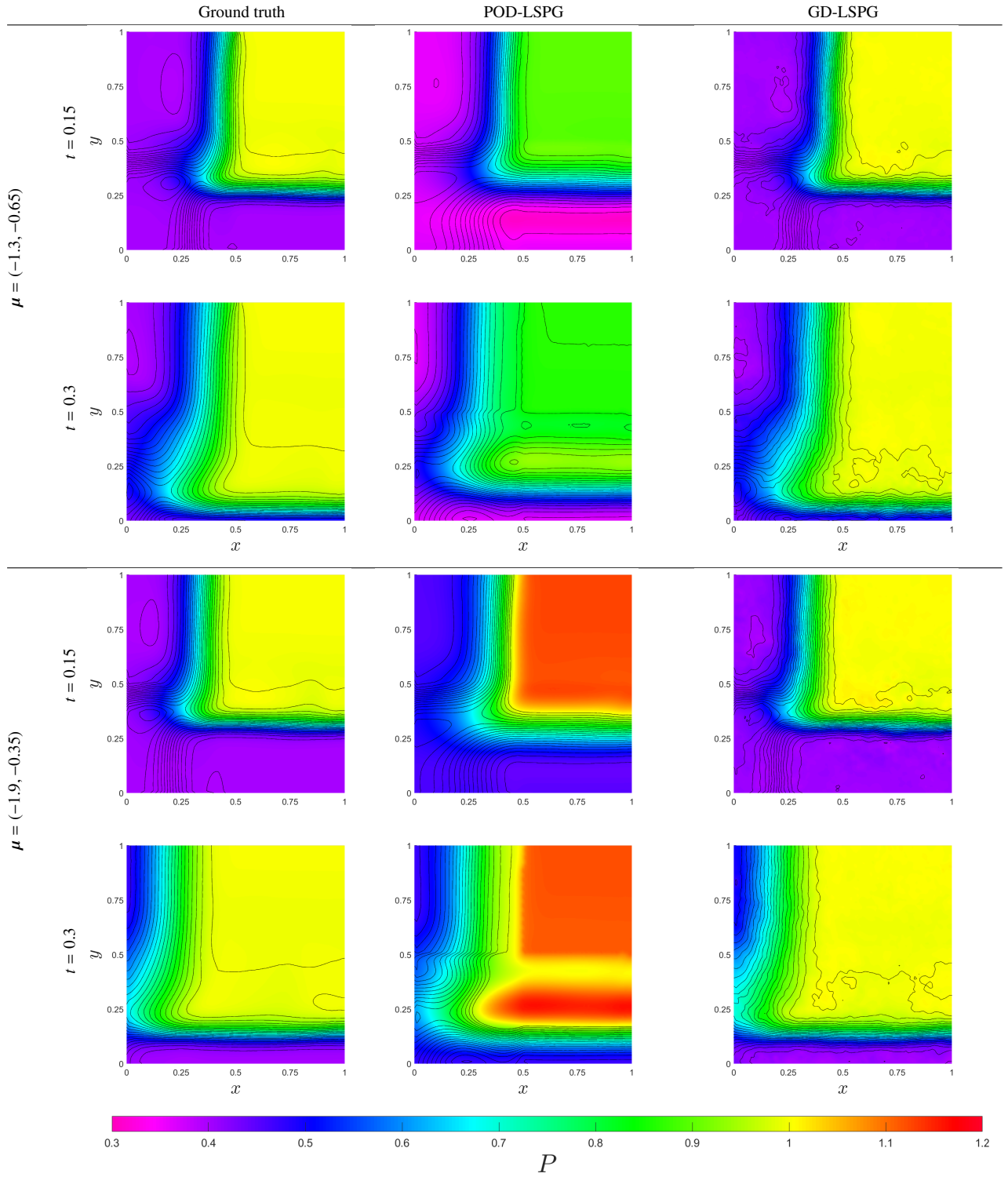


Figure 13: Ground truth, POD-LSPG, and GD-LSPG ROM solutions to the 2D Euler equations at time $t = 0.15$ and $t = 0.3$ for two test parameter sets $\mu = (\mu_u = -1.3, \mu_v = -0.65)$ and $\mu = (\mu_u = -1.9, \mu_v = -0.35)$, respectively. The ROMs are constructed using a latent space dimension of $M = 3$. Note POD-LSPG's inability to model the shock behavior, leading to a diffusive and inaccurate solution that does not accurately model the advection-driven behavior of the problem. Alternatively, GD-LSPG models the shock behavior with much higher accuracy. (Online version in color.)

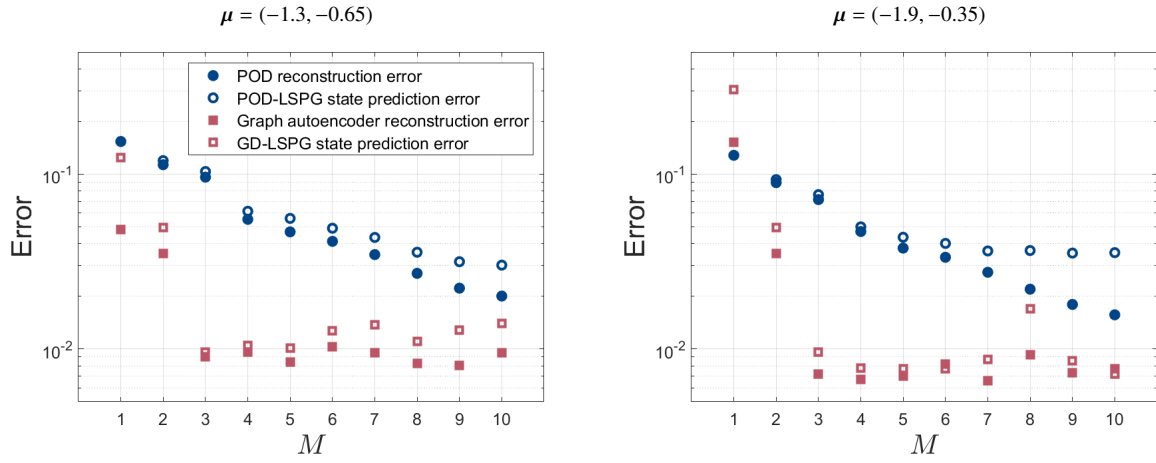


Figure 14: POD reconstruction error, graph autoencoder reconstruction error, POD-LSPG, and GD-LSPG state prediction error plotted with respect to the dimension of the low-dimensional latent space, M . The two plots represent the results for two choices of test parameter sets. For small latent space dimensions, GD-LSPG outperforms POD-LSPG in terms of accuracy. (Online version in color.)

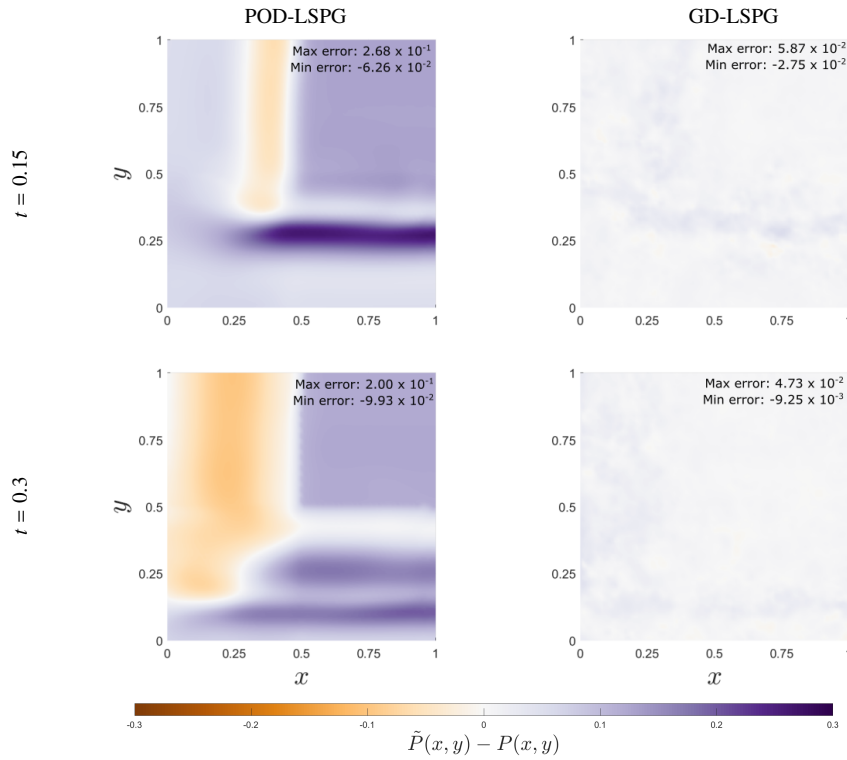


Figure 15: The left column presents the local ROM errors for GD-LSPG, while the right column presents that of POD-LSPG. Both POD-LSPG and GD-LSPG have latent space dimension $M = 3$ and the results are depicted for the parameter set $\mu = (\mu_u = -1.9, \mu_v = -0.35)$. We define local error to be $\tilde{P}(x, y) - P(x, y)$ at a given time step. The POD-LSPG solution fails to accurately model the advection-driven nature of the solution and shows errors as high as 25% in some parts of the domain. GD-LSPG, alternatively, models the shock wave much more accurately and has only small errors very close to the shock. This solution behavior near the shock indicates that GD-LSPG's errors are primarily a result of the shocks in the GD-LSPG solution being slightly out of phase from that of the FOM solution. (Online version in color.)

6. Conclusions and future work

In this paper, we present GD-LSPG, a PMOR method that leverages a graph autoencoder architecture to perform PMOR on unstructured meshes; a setting where traditional CNN-based dLSPG is not directly applicable. The graph autoencoder is constructed by first generating a hierarchy of reduced graphs to emulate the compressive capabilities of CNNs. Next, message passing operations are trained for each layer in the hierarchy of reduced graphs to emulate the filtering capabilities of CNNs. In an online stage, the graph autoencoder is coupled with the same time integration scheme deployed by dLSPG to perform time integration and generate solutions for parameter sets not seen during training. To benchmark the accuracy of GD-LSPG against other methods, we compare directly the solutions for a 1D Burgers' equation problem with a structured mesh generated by GD-LSPG to those generated by the CNN-based dLSPG [46, 47] and POD-LSPG [25, 70] frameworks. The results of this study find that, while GD-LSPG does not perform as well as traditional CNN-based dLSPG for structured meshes, GD-LSPG still provides significant improvement over the affine POD-LSPG framework. To demonstrate the flexibility of GD-LSPG in a setting where dLSPG is not directly applicable, we test GD-LSPG on a 2D Euler equations model deploying an unstructured mesh and find that, for small latent spaces, GD-LSPG significantly outperforms the POD-LSPG solution in terms of accuracy.

One possible future direction is to develop a hyper-reduction scheme to achieve cost savings. In GD-LSPG's current formulation, the high-dimensional residual must be computed and projected onto the low-dimensional latent space, forcing the operational count complexity to scale on the dimension of the FOM. A hyper-reduction scheme would overcome this limitation by sampling and generating a sparse representation of the high-dimensional residual, thereby eliminating an operational count complexity that scales on the dimension of the FOM. To date, hyper-reduction has been achieved for dLSPG using shallow decoders [48]. However, GD-LSPG uses a deep decoder. As a result, we leave this as an open area of investigation.

This paper aims primarily to investigate GD-LSPG in the context of advection-dominated flows modeled by unstructured meshes for simple geometries to provide a baseline and proof of concept. As a result, another open area of interest is to apply GD-LSPG to domains with more complicated geometries, such as airfoils and nozzles, where unstructured meshes can be advantageous.

7. Acknowledgements

L. K. Magargal is supported by the Department of Defense (DoD) through the National Defense Science & Engineering Graduate (NDSEG) Fellowship Program. L. K. Magargal and J. W. Jaworski acknowledge the financial support of the Department of Energy under grant DE-EE0008964. S. N. Rodriguez and J. G. Michopoulos acknowledge the support of the Office of Naval Research through U.S. Naval Research Laboratory core funding. J. W. Jaworski acknowledges the partial support of the National Science Foundation under CAREER award 1846852.

Appendix A. Architecture details and training

The autoencoders are trained with the strategies outlined in this section. All models are trained on an NVIDIA L40S GPU. We initialize all weights and biases using Xavier initialization [88]. Furthermore, all finite difference Jacobians are approximated using a step size of 0.01.

To train the graph autoencoder in the 1D Burgers' equation model, we first perform a training/validation split, where 4000 solution states are stored for validation, and the remaining 36,080 solution states are used for training. We train the model for 1000 epochs where, at each epoch, the training set is passed through the autoencoder in batches of 20. Loss is evaluated using (25) with a regularization parameter $\lambda = 0.001$. The Adam optimizer [78] is deployed with a learning rate of 10^{-4} . The exact details of the autoencoder architecture are provided in Tables A.1 and A.2. Activation functions are taken to be ELU [65]. Empirically, we noticed that the architecture struggles to model the solution state near the boundaries, especially when the shock approaches the boundary. We believe that this challenge is related to the nonlocality of our graph autoencoder, as the boundary nodes do not receive adequate and appropriate information from the space outside of the domain. This behavior is often found across the field of nonlocal modeling, including peridynamics [89] and smoothed-particle hydrodynamics [90]. We leave this as an open area for future investigation, but for now, we present a simple procedure for including padding in a graph autoencoder. This procedure appends 30 nodes to the left side of the domain and sets their features to be the value of the left boundary condition, i.e., μ_1 . Along the right boundary, we find that solving Burgers' equation with the finite volume solver for 30 finite volume cells to the right of the right boundary and prescribing the computed velocity values to the features of the padding nodes is appropriate. Our decoder reconstructs the solution for the nodes in the physical domain as well as those in the padding zones but only computes the loss with respect to the nodes in the physical domain of the problem. During the hierarchical spectral clustering algorithm, radius r^i for layer i is chosen such that (6) gives roughly 7 edges for each node, i.e., $r^i = (x_{\text{right}} - x_{\text{left}}) \left(\frac{7}{2|\mathcal{V}^i|} \right)$, where $x_{\text{right}} \in \mathbb{R}$ is the position of the rightmost padding node in \mathcal{V}^0 and $x_{\text{left}} \in \mathbb{R}$ is the position of the leftmost padding node in \mathcal{V}^0 .

To train the CNN-based autoencoders deployed in the 1D Burgers' equation model, we first perform a training/validation split, where 4000 solution states are stored for validation, and the remaining 36,080 solution states are used for training. We train the model for 1000 epochs where, at each epoch, the training set is passed through the autoencoder in batches of 20. Loss is evaluated using (25) with a regularization parameter $\lambda = 0$ (i.e., no Jacobian regularization) and stochastic gradient descent is performed using the Adam optimizer [78] to update the weights and biases at each epoch. The learning rate is chosen to be 10^{-4} . The exact details of the autoencoders are provided in Tables A.3 and A.4. Activation functions are taken to be ELU [65]. A kernel size of 25 is chosen at each layer, where half-padding is used. In the decoder, the transposed convolution layers are given an output padding of 1.

To train the graph autoencoders used in the 2D Euler equations model, we first perform a training/validation split, where 525 solution states are stored for validation, and the remaining 7000 solution states are used for training. We train the model for 5000 epochs where, at each epoch, the training set is passed through the autoencoder in batches of 20. Loss is evaluated using (25) with a regularization parameter $\lambda = 0.001$ and stochastic gradient descent is performed using the Adam optimizer [78] to update the weights and biases at each epoch. The learning rate is chosen to be 10^{-4} . Activation functions are taken to be ELU [65]. To compute the hierarchy of reduced graphs, at each layer, (6) uses a radius that aims for 9 edges for each node, i.e., $r^i = \sqrt{\frac{9}{\pi|\mathcal{V}^i|}}$. Exact details of the graph autoencoder architecture are in Tables A.5 and A.6.

We found stacking message passing operations to be beneficial to the accuracy of the graph autoencoder. In the MPP layers, we perform message passing operations multiple times before pooling. In the UMP layers, multiple message passing operations are performed after unpooling. The number of message passing operations is represented

in Tables A.1, A.2, A.5, and A.6 under the “# of MP operations” column. Lastly, the last message passing operation of the decoder does not have an activation function associated with it, as the range of the ELU activation function does not match the domain of the state variables.

Appendix A.1. Details of the graph autoencoder for 1D Burgers' equation model

Table A.1: Outputs of each layer of the encoder of the graph autoencoder for 1D Burgers' equation model. The input vector length includes the 30 padding nodes on both sides of the domain. Parentheses in '# of MP operations' column denote the number of features in the output of intermediate message passing operations.

Encoder details					
i	Layer type	$ \mathcal{V}^i $	N_F^i	# of MP operations	Vector length
0	Preprocessing	316	1	N/A	N/A
1	MPP	64	8	2 (8)	N/A
2	MPP	16	16	2 (16)	N/A
3	MPP	4	32	2 (32)	N/A
4	MPP	2	64	2 (64)	N/A
5	MLP _{enc}	N/A	N/A	N/A	M

Table A.2: Outputs of each layer of the decoder of the graph autoencoder for 1D Burgers' equation model. The output vector length includes the 30 padding nodes on both sides of the domain. Parentheses in '# of MP operations' column denote the number of features in the output of intermediate message passing operations.

Decoder details					
i	Layer type	$ \mathcal{V}^i $	N_F^i	# of MP operations	Vector length
0	MLP _{dec}	2	64	N/A	N/A
1	UMP	4	32	2 (64)	N/A
2	UMP	16	16	2 (32)	N/A
3	UMP	64	8	2 (16)	N/A
4	UMP	316	1	2 (8)	N/A
5	Postprocessing	N/A	N/A	N/A	316

Appendix A.2. Details of the CNN-based autoencoder for 1D Burgers' equation model

Table A.3: Outputs of each layer of the encoder of the CNN-based autoencoder for 1D Burgers' equation model. Note: the MLP_{dec} in the CNN-based autoencoder is followed by an ELU activation function (unlike the graph autoencoder). Empirically, we found the activation function slightly improves accuracy for the CNN-based autoencoder, but not the graph autoencoder.

Encoder details					
i	Layer type	Grid points	Channels	Stride	Vector length
0	Preprocessing	256	256	N/A	N/A
1	1D Convolution	128	8	2	N/A
2	1D Convolution	32	16	4	N/A
3	1D Convolution	8	32	4	N/A
4	1D Convolution	2	64	4	N/A
5	MLP_{enc}	N/A	N/A	N/A	M

Table A.4: Outputs of each layer of the decoder of the CNN-based autoencoder for 1D Burgers' equation model.

Decoder details					
i	Layer type	Grid points	Channels	Stride	Vector length
0	MLP_{dec}	2	64	N/A	N/A
1	1D Transposed Convolution	8	32	4	N/A
2	1D Transposed Convolution	32	16	4	N/A
3	1D Transposed Convolution	128	8	4	N/A
4	1D Transposed Convolution	256	1	2	N/A
5	Postprocessing	N/A	N/A	N/A	256

Appendix A.3. Details of the graph autoencoder for 2D Riemann Problem

Table A.5: Outputs of each layer of the encoder of the graph autoencoder for 2D Euler equations model. Parentheses in ‘# of MP operations’ column denote the number of features in the output of intermediate message passing operations.

Encoder details					
i	Layer type	$ \mathcal{V}^i $	N_F^i	# of MP operations	Vector length
0	Preprocessing	4328	4	N/A	N/A
1	MPP	512	16	2 (16)	N/A
2	MPP	64	64	2 (64)	N/A
3	MPP	8	128	2 (128)	N/A
4	MPP	2	256	2 (256)	N/A
5	MLP _{enc}	N/A	N/A	N/A	M

Table A.6: Outputs of each layer of the decoder of the graph autoencoder for 2D Euler equations model. Parentheses in ‘# of MP operations’ column denote the number of features in the output of intermediate message passing operations.

Decoder details					
i	Layer type	$ \mathcal{V}^i $	N_F^i	# of MP operations	Vector length
0	MLP _{dec}	2	256	N/A	N/A
1	UMP	8	128	2 (256)	N/A
2	UMP	64	64	2 (128)	N/A
3	UMP	512	16	2 (64)	N/A
4	UMP	4328	4	2 (16)	N/A
5	Postprocessing	N/A	N/A	N/A	4328×4

Appendix B. Proper orthogonal decomposition

To compute the set of orthonormal POD basis vectors, we use the method of snapshots [5] in which a snapshot matrix of the time history of the FOM solutions is generated, $\mathbf{X}^{\text{POD}} = [\mathbf{x}^1, \dots, \mathbf{x}^{n_{\text{train}}}] \in \mathbb{R}^{N \times N_{\text{train}}}$, where $N_{\text{train}} \in \mathbb{N}$ is the number of training snapshots, \mathbf{x}^i is the solution state vector of snapshot i , and N is the dimension of the state vector. Next, singular value decomposition is performed on the snapshot matrix, \mathbf{X}^{POD} :

$$\mathbf{X}^{\text{POD}} = \mathbf{V}\mathbf{\Sigma}\mathbf{U}^T \quad (\text{B.1})$$

where $\mathbf{V} = [\mathbf{v}_1, \dots, \mathbf{v}_N] \in \mathbb{R}^{N \times N}$ is a matrix of N orthonormal vectors which represent the POD modes in the order of decreasing singular values, $\mathbf{\Sigma} = \text{diag}(\sigma_1, \dots, \sigma_N) \in \mathbb{R}^{N \times N}$ is the diagonal matrix of singular values ordered as $\sigma_1 \geq \dots \geq \sigma_N$, and $\mathbf{U} = [\mathbf{u}_1, \dots, \mathbf{u}_{n_s}] \in \mathbb{R}^{N_{\text{train}} \times N_{\text{train}}}$ provides information about the time dynamics. The POD basis is created by truncating the first M left singular vectors of the snapshot matrix, i.e., $\mathbf{\Phi} = [\mathbf{v}_1, \dots, \mathbf{v}_M] \in \mathbb{R}^{N \times M}$, which is made up of M orthonormal vectors that describe the dominant mode shapes of the system. The POD basis vectors are both optimal in the L^2 sense and orthonormal, making the POD basis a common choice for deployment in the context of PMOR [91].

References

- [1] R. J. LeVeque, *Finite volume methods for hyperbolic problems*, Cambridge Texts in Applied Mathematics, Cambridge University Press, Cambridge, UK, 2002.
- [2] S. Mazumder, *Numerical methods for partial differential equations: finite difference and finite volume methods*, Academic Press, Cambridge, MA, 2015.
- [3] P. Benner, S. Gugercin, K. Willcox, A survey of projection-based model reduction methods for parametric dynamical systems, *SIAM Review* 57 (4) (2015) 483–531.
- [4] M. Bern, P. Plassmann, Chapter 6 - mesh generation, in: J. Sack, J. Urrutia (Eds.), *Handbook of Computational Geometry*, North-Holland, Amsterdam, 2000, pp. 291–332.
- [5] L. Sirovich, Turbulence and the dynamics of coherent structures part I: coherent structures, *Quarterly of Applied Mathematics* 45 (3) (1987) 561–571.
- [6] U. Baur, C. Beattie, P. Benner, S. Gugercin, Interpolatory projection methods for parameterized model reduction, *SIAM Journal on Scientific Computing* 33 (5) (2011) 2489–2518.
- [7] B. Moore, Principal component analysis in linear systems: controllability, observability, and model reduction, *IEEE Transactions on Automatic Control* 26 (1) (1981) 17–32.
- [8] S. E. Ahmed, O. San, Breaking the Kolmogorov barrier in model reduction of fluid flows, *Fluids* 5 (1) (2020).
- [9] N. Franco, A. Manzoni, P. Zunino, A deep learning approach to reduced order modelling of parameter dependent partial differential equations, *Mathematics of Computation* 92 (340) (2023) 483–524.
- [10] B. Peherstorfer, Model reduction for transport-dominated problems via online adaptive bases and adaptive sampling, *SIAM Journal on Scientific Computing* 42 (5) (2020) A2803–A2836.
- [11] B. Peherstorfer, Breaking the Kolmogorov barrier with nonlinear model reduction, *Notices of the American Mathematical Society* 69 (5) (2022) 725–733.
- [12] G. Welper, Interpolation of functions with parameter dependent jumps by transformed snapshots, *SIAM Journal on Scientific Computing* 39 (4) (2017) A1225–A1250.
- [13] M. Dihlmann, M. Drohmann, B. Haasdonk, Model reduction of parametrized evolution problems using the reduced basis method with adaptive time partitioning, in: *Proceedings of the International Conference on Adaptive Modeling and Simulation*, 2011.
- [14] M. Drohmann, B. Haasdonk, M. Ohlberger, Adaptive reduced basis methods for nonlinear convection–diffusion equations, in: *Finite Volumes for Complex Applications VI Problems & Perspectives: FVCA 6*, International Symposium, Prague, Springer, 2011, pp. 369–377.
- [15] M. Ohlberger, S. Rave, Nonlinear reduced basis approximation of parameterized evolution equations via the method of freezing, *Comptes Rendus Mathématique* 351 (23–24) (2013) 901–906.
- [16] D. Amsallem, M. J. Zahr, C. Farhat, Nonlinear model order reduction based on local reduced-order bases, *International Journal for Numerical Methods in Engineering* 92 (10) (2012) 891–916.
- [17] R. Geelen, S. Wright, K. Willcox, Operator inference for non-intrusive model reduction with quadratic manifolds, *Computer Methods in Applied Mechanics and Engineering* 403 (2023) 115717.
- [18] J. Barnett, C. Farhat, Quadratic approximation manifold for mitigating the Kolmogorov barrier in nonlinear projection-based model order reduction, *Journal of Computational Physics* (2022) 111348.
- [19] N. J. Nair, M. Balajewicz, Transported snapshot model order reduction approach for parametric, steady-state fluid flows containing parameter-dependent shocks, *International Journal for Numerical Methods in Engineering* 117 (12) (2019) 1234–1262.
- [20] P. Benner, M. Ohlberger, A. Cohen, K. Willcox, *Model reduction and approximation*, Society for Industrial and Applied Mathematics, Philadelphia, PA, 2017.
- [21] A. Antoulas, *Approximation of large-scale dynamical systems*, Society for Industrial and Applied Mathematics, Philadelphia, PA, 2009.
- [22] M. Barrault, Y. Maday, N. C. Nguyen, A. T. Patera, An ‘empirical interpolation’ method: application to efficient reduced-basis discretization of partial differential equations, *Comptes Rendus Mathématique* 339 (9) (2004) 667–672.
- [23] S. Chaturantabut, D. C. Sorensen, Nonlinear model reduction via discrete empirical interpolation, *SIAM Journal on Scientific Computing* 32 (5) (2010) 2737–2764.
- [24] Z. Drmac, S. Gugercin, A new selection operator for the discrete empirical interpolation method—improved a priori error bound and extensions, *SIAM Journal on Scientific Computing* 38 (2) (2016) A631–A648.
- [25] K. Carlberg, C. Bou-Mosleh, C. Farhat, Efficient non-linear model reduction via a least-squares Petrov–Galerkin projection and compressive tensor approximations, *International Journal for Numerical Methods in Engineering* 86 (2) (2011) 155–181.
- [26] K. Carlberg, C. Farhat, J. Cortial, D. Amsallem, The GNAT method for nonlinear model reduction: effective implementation and application to computational fluid dynamics and turbulent flows, *Journal of Computational Physics* 242 (2013) 623–647.
- [27] C. Farhat, T. Chapman, P. Avery, Structure-preserving, stability, and accuracy properties of the energy-conserving sampling and weighting method for the hyper reduction of nonlinear finite element dynamic models, *International Journal for Numerical Methods in Engineering* 102 (5) (2015) 1077–1110.
- [28] B. Peherstorfer, K. Willcox, Data-driven operator inference for nonintrusive projection-based model reduction, *Computer Methods in Applied Mechanics and Engineering* 306 (2016) 196–215.
- [29] P. Benner, P. Goyal, B. Kramer, B. Peherstorfer, K. Willcox, Operator inference for non-intrusive model reduction of systems with non-polynomial nonlinear terms, *Computer Methods in Applied Mechanics and Engineering* 372 (2020) 113433.
- [30] S. A. McQuarrie, C. Huang, K. E. Willcox, Data-driven reduced-order models via regularised operator inference for a single-injector combustion process, *Journal of the Royal Society of New Zealand* 51 (2) (2021) 194–211.
- [31] E. Qian, B. Kramer, B. Peherstorfer, K. Willcox, Lift & Learn: physics-informed machine learning for large-scale nonlinear dynamical systems, *Physica D: Nonlinear Phenomena* 406 (2020) 132401.
- [32] P. Khodabakhshi, K. E. Willcox, Non-intrusive data-driven model reduction for differential–algebraic equations derived from lifting transformations, *Computer Methods in Applied Mechanics and Engineering* 389 (2022) 114296.

- [33] D. Bank, N. Koenigstein, R. Giryas, Autoencoders, *Machine learning for data science handbook: data mining and knowledge discovery handbook* (2023) 353–374.
- [34] K. Hasegawa, K. Fukami, T. Murata, K. Fukagata, Machine-learning-based reduced-order modeling for unsteady flows around bluff bodies of various shapes, *Theoretical and Computational Fluid Dynamics* 34 (4) (2020) 367–383.
- [35] S. Wiewel, M. Becher, N. Thuerey, Latent space physics: Towards learning the temporal evolution of fluid flow, *Computer Graphics Forum* 38 (2) (2019) 71–82.
- [36] B. Kim, V. C. Azevedo, N. Thuerey, T. Kim, M. Gross, B. Solenthaler, Deep fluids: A generative network for parameterized fluid simulations, in: *Computer Graphics Forum*, Vol. 38, Wiley Online Library, 2019, pp. 59–70.
- [37] R. Maulik, B. Lusch, P. Balaprakash, Reduced-order modeling of advection-dominated systems with recurrent neural networks and convolutional autoencoders, *Physics of Fluids* 33 (3) (2021) 037106.
- [38] S. Fresca, L. Dede, A. Manzoni, A comprehensive deep learning-based approach to reduced order modeling of nonlinear time-dependent parametrized PDEs, *Journal of Scientific Computing* 87 (2) (2021) 1–36.
- [39] S. Dutta, P. Rivera-Casillas, B. Styles, M. W. Farthing, Reduced order modeling using advection-aware autoencoders, *Mathematical and Computational Applications* 27 (3) (2022).
- [40] R. T. Chen, Y. Rubanova, J. Bettencourt, D. K. Duvenaud, Neural ordinary differential equations, *Advances in neural information processing systems* 31 (2018).
- [41] C. Finlay, J.-H. Jacobsen, L. Nurbekyan, A. Oberman, How to train your neural ODE: the world of Jacobian and kinetic regularization, in: *International Conference on Machine Learning*, 2020, pp. 3154–3164.
- [42] Y. Lu, A. Zhong, Q. Li, B. Dong, Beyond finite layer neural networks: Bridging deep architectures and numerical differential equations, in: *Proceedings of the 35th International Conference on Machine Learning*, 2018, pp. 3276–3285.
- [43] M. Raissi, P. Perdikaris, G. Karniadakis, Physics-informed neural networks: a deep learning framework for solving forward and inverse problems involving nonlinear partial differential equations, *Journal of Computational Physics* 378 (2019) 686–707.
- [44] D. Hartman, L. K. Mestha, A deep learning framework for model reduction of dynamical systems, in: *2017 IEEE Conference on Control Technology and Applications (CCTA)*, 2017, pp. 1917–1922.
- [45] K. Kashima, Nonlinear model reduction by deep autoencoder of noise response data, in: *2016 IEEE 55th Conference on Decision and Control (CDC)*, IEEE, 2016, pp. 5750–5755.
- [46] K. Lee, K. T. Carlberg, Model reduction of dynamical systems on nonlinear manifolds using deep convolutional autoencoders, *Journal of Computational Physics* 404 (2020) 108973.
- [47] K. Lee, K. T. Carlberg, Deep conservation: A latent-dynamics model for exact satisfaction of physical conservation laws, in: *Proceedings of the AAAI Conference on Artificial Intelligence*, Vol. 35, 2021, pp. 277–285.
- [48] Y. Kim, Y. Choi, D. Widemann, T. Zohdi, A fast and accurate physics-informed neural network reduced order model with shallow masked autoencoder, *Journal of Computational Physics* 451 (2022) 110841.
- [49] P. W. Battaglia, J. B. Hamrick, V. Bapst, A. Sanchez-Gonzalez, V. Zambaldi, M. Malinowski, A. Tacchetti, D. Raposo, A. Santoro, R. Faulkner, et al., Relational inductive biases, deep learning, and graph networks, *arXiv preprint arXiv:1806.01261* (2018).
- [50] J. Zhou, G. Cui, S. Hu, Z. Zhang, C. Yang, Z. Liu, L. Wang, C. Li, M. Sun, Graph neural networks: A review of methods and applications, *AI Open* 1 (2020) 57–81.
- [51] S. Barwey, V. Shankar, V. Viswanathan, R. Maulik, Multiscale graph neural network autoencoders for interpretable scientific machine learning, *Journal of Computational Physics* 495 (2023) 112537.
- [52] F. Pichi, B. Moya, J. S. Hesthaven, A graph convolutional autoencoder approach to model order reduction for parametrized PDEs, *Journal of Computational Physics* 501 (2024) 112762.
- [53] H. Gao, S. Ji, Graph U-nets, in: *International Conference on Machine Learning*, 2019, pp. 2083–2092.
- [54] P. Y. Chen, J. Xiang, D. H. Cho, G. Pershing, H. T. Maia, M. Chiamonte, K. Carlberg, E. Grinspun, CROM: continuous reduced-order modeling of PDEs using implicit neural representations, *arXiv preprint arXiv:2206.02607* (2022).
- [55] H. Eivazi, S. Le Clainche, S. Hoyas, R. Vinuesa, Towards extraction of orthogonal and parsimonious non-linear modes from turbulent flows, *Expert Systems with Applications* 202 (2022) 117038.
- [56] S. Pan, S. L. Brunton, J. N. Kutz, Neural implicit flow: a mesh-agnostic dimensionality reduction paradigm of spatio-temporal data, *Journal of Machine Learning Research* 24 (41) (2023) 1–60.
- [57] K. Fukami, T. Nakamura, K. Fukagata, Convolutional neural network based hierarchical autoencoder for nonlinear mode decomposition of fluid field data, *Physics of Fluids* 32 (9) (2020) 095110.
- [58] W. L. Hamilton, *Graph representation learning*, Morgan & Claypool Publishers, San Rafael, CA, 2020.
- [59] P. Bongini, M. Bianchini, F. Scarselli, Molecular generative graph neural networks for drug discovery, *Neurocomputing* 450 (2021) 242–252.
- [60] M. E. Newman, D. J. Watts, S. H. Strogatz, Random graph models of social networks, *Proceedings of the National Academy of Sciences* 99 (2002) 2566–2572.
- [61] B. Rennie, A. Dobson, On Stirling numbers of the second kind, *Journal of Combinatorial Theory* 7 (2) (1969) 116–121.
- [62] U. Von Luxburg, A tutorial on spectral clustering, *Statistics and Computing* 17 (2007) 395–416.
- [63] J. MacQueen, Some methods for classification and analysis of multivariate observations, in: *Proceedings of the Fifth Berkeley Symposium on Mathematical Statistics and Probability*, 1967, pp. 281–297.
- [64] W. Hamilton, Z. Ying, J. Leskovec, Inductive representation learning on large graphs, *Advances in Neural Information Processing Systems* 30 (2017).
- [65] D.-A. Clevert, T. Unterthiner, S. Hochreiter, Fast and accurate deep network learning by exponential linear units (ELUs), in: *International Conference on Learning Representations (ICLR)*, 2016.
- [66] E. Dupont, A. Doucet, Y. W. Teh, Augmented neural ODEs, *Advances in Neural Information Processing Systems* 32 (2019).
- [67] S. Josias, W. Brink, Jacobian norm regularisation and conditioning in neural ODEs, in: *Southern African Conference for Artificial Intelligence Research*, Springer, 2022, pp. 31–45.
- [68] S. Fresca, A. Manzoni, POD-DL-ROM: Enhancing deep learning-based reduced order models for nonlinear parametrized PDEs by proper

- orthogonal decomposition, *Computer Methods in Applied Mechanics and Engineering* 388 (2022) 114181.
- [69] F. Regazzoni, L. Dedè, A. Quarteroni, Machine learning for fast and reliable solution of time-dependent differential equations, *Journal of Computational Physics* 397 (2019) 108852.
 - [70] K. Carlberg, M. Barone, H. Antil, Galerkin v. least-squares Petrov-Galerkin projection in nonlinear model reduction, *Journal of Computational Physics* 330 (2017) 693–734.
 - [71] J. Nocedal, S. J. Wright, *Numerical optimization*, Springer, New York, NY, 1999.
 - [72] J. Barnett, C. Farhat, Y. Maday, Neural-network-augmented projection-based model order reduction for mitigating the Kolmogorov barrier to reducibility, *Journal of Computational Physics* 492 (2023) 112420.
 - [73] M. J. Rewieński, A trajectory piecewise-linear approach to model order reduction of nonlinear dynamical systems, Ph.D. thesis, Massachusetts Institute of Technology (2003).
 - [74] A. Kurganov, E. Tadmor, Solution of two-dimensional Riemann problems for gas dynamics without Riemann problem solvers, *Numerical Methods for Partial Differential Equations: An International Journal* 18 (5) (2002) 584–608.
 - [75] R. Liska, B. Wendroff, Comparison of several difference schemes on 1D and 2D test problems for the Euler equations, *SIAM Journal on Scientific Computing* 25 (3) (2003) 995–1017.
 - [76] A. Paszke, S. Gross, F. Massa, A. Lerer, J. Bradbury, G. Chanan, T. Killeen, Z. Lin, N. Gimelshein, L. Antiga, et al., Pytorch: an imperative style, high-performance deep learning library, *Advances in Neural Information Processing Systems* 32 (2019).
 - [77] M. Fey, J. E. Lenssen, Fast graph representation learning with PyTorch Geometric, arXiv preprint arXiv:1903.02428 (2019).
 - [78] D. P. Kingma, J. Ba, Adam: A method for stochastic optimization, arXiv preprint arXiv:1412.6980 (2014).
 - [79] H. Nishikawa, K. Kitamura, Very simple, carbuncle-free, boundary-layer-resolving, rotated-hybrid Riemann solvers, *Journal of Computational Physics* 227 (4) (2008) 2560–2581.
 - [80] S. J. Paardekooper, Multidimensional upwind hydrodynamics on unstructured meshes using graphics processing units—I. Two-dimensional uniform meshes, *Monthly Notices of the Royal Astronomical Society* 469 (4) (2017) 4306–4340.
 - [81] Y.-X. Ren, A robust shock-capturing scheme based on rotated Riemann solvers, *Computers & Fluids* 32 (10) (2003) 1379–1403.
 - [82] P. Roe, Approximate Riemann solvers, parameter vectors, and difference schemes, *Journal of Computational Physics* 43 (2) (1981) 357–372.
 - [83] C.-W. Shu, S. Osher, Efficient implementation of essentially non-oscillatory shock-capturing schemes, *Journal of Computational Physics* 77 (2) (1988) 439–471.
 - [84] C. W. Schulz-Rinne, J. P. Collins, H. M. Glaz, Numerical solution of the Riemann problem for two-dimensional gas dynamics, *SIAM Journal on Scientific Computing* 14 (6) (1993) 1394–1414.
 - [85] P. D. Lax, X.-D. Liu, Solution of two-dimensional Riemann problems of gas dynamics by positive schemes, *SIAM Journal on Scientific Computing* 19 (2) (1998) 319–340.
 - [86] S. K. Lam, A. Pitrou, S. Seibert, Numba: A LLVM-based Python JIT compiler, in: *Proceedings of the Second Workshop on the LLVM Compiler Infrastructure in HPC*, 2015, pp. 1–6.
 - [87] C. Geuzaine, J.-F. Remacle, Gmsh: a 3-D finite element mesh generator with built-in pre-and post-processing facilities, *International Journal for Numerical Methods in Engineering* 79 (11) (2009) 1309–1331.
 - [88] X. Glorot, Y. Bengio, Understanding the difficulty of training deep feedforward neural networks, in: *Proceedings of the Thirteenth International Conference on Artificial Intelligence and Statistics, JMLR Workshop and Conference Proceedings*, 2010, pp. 249–256.
 - [89] E. Madenci, E. Oterkus, *Peridynamic theory and its applications*, Springer, New York, 2013.
 - [90] J. J. Monaghan, Smoothed particle hydrodynamics, *Annual Review of Astronomy and Astrophysics* 30 (1992) 543–574.
 - [91] K. Taira, S. L. Brunton, S. T. M. Dawson, C. W. Rowley, T. Colonius, B. J. McKeon, O. T. Schmidt, S. Gordyeyev, V. Theofilis, L. S. Ukeiley, Modal analysis of fluid flows: an overview, *AIAA Journal* 55 (12) (2017) 4013–4041.